Stony Brook University

Fabrication of a novel biosensor for macromolecules detection through molecular imprinting technique

by

Yingjie Yu

to

The Graduate School

in Partial Fulfillment of the

Requirements

for the Degree of

Doctor of Philosophy

in

Materials Science and Engineering

Stony Brook University

May 2016

Stony Brook University

The Graduate School

Yingjie Yu

We, the dissertation committee for the above candidate for the

Doctor of Philosophy degree, hereby recommend

acceptance of this dissertation.

Dr. Miriam Rafailovich – Dissertation Advisor
Distinguished professor of Department of Materials Science and Engineering
Stony Brook University

Dr. Jonathon Sokolov - Chairperson of Defense
Professor of Department of Materials Science and Engineering
Stony Brook University

Dr. Macia Simon
Professor of Department of Oral Biology and Pathology
Stony Brook University

Dr. Kalle Levon
Professor of Department of Chemical and Biomolecular Engineering
NYU Tandon School of Engineering

This dissertation is accepted by the Graduate School

Charles Taber
Dean of the Graduate School

Abstract of the Dissertation

Fabrication of a novel biosensor for macromolecules detection through molecular imprinting technique

by

Yingjie Yu

Doctor of Philosophy

in

Materials Science and Engineering

Stony Brook University

2016

There is an increasing need for precise molecular detection as a diagnostic tool for early identification of diseases, pathogens, and abnormal protein levels in the body. Typical chemical analytical methods are generally costly, unstable, and time-consuming. Molecular imprinting (MI) technique，based on the “lock and key model”, could be a simple method to overcome those shortcomings. In this study, a self-assembled monolayer (SAM) was employed as a platform to fabricate MI biosensor for detection of macromolecules. I demonstrated that, when the monolayer was formed on a rough surface, this method was in fact templating molecules in three dimensions, and hence was not limited by the height of the monolayer, but rather by the height of the roughness.

This hypothesis was tested on biomolecules of multiple length scales. The SAM is assembled on the walls of the niche, forming a 3D pattern of the analyte uniquely molded to its

contour. The surfaces with multi-scale roughness were prepared by evaporation of gold onto electropolished (smooth) and unpolished (rough) Si wafers, where the native roughness was found to have a normal distribution centered around 5 and 90 nm respectively. Our studies, using molecules, such as proteins, i.e., hemoglobin, ranging from a few nanometers, to viruses (i.e. polio, adenovirus), ranging from several tens of nanometers, and protein complexes ranging from several hundred nanometers, showed that when the size of the analyte matched the roughness of the gold surface, this method was very effective and could detect even small changes in the configuration, such as those induced by changes in the pH of the system.

The detection method was further quantified by applying it to the detection of CEA in pancreatic cyst fluid obtained from 18 patients under IRB 95867-6. The results of the MI biosensor were directly compared with those obtained using ELISA in the hospital pathology laboratory with excellent agreement, except that the MI biosensor used only 1% of the volume of the ELISA test and produced results in less than 5 minutes, as compared to at least 10 hours.

Table of Contents

List of Figures and Tables

Chapter 1 Introduction

1.1 Background of biosensors

There is an increasing need for precise molecular detection as a diagnostic tool for early identification of diseases, pathogens, and abnormal protein levels in the body. Biosensors serve as low-cost and highly efficient devices for the purpose of detecting different molecules. A biosensor is an analytical device, used for the detection of an analyte, that combines a biological component with a detector.**[1, 2]** The biosensor is composed to 2 critical parts: a bio-element and a sensor-element. The basic setup for biosensor operation is shown in Fig. 1-1. A specific analyte, such as a protein, recognizes a specific bio-element and the biosensor transduces the change in the biomolecule into an electrical signal. Biosensor detection, as a one step process, is reproducible, accurate, and requires much shorter response time compared to traditional bioanalytical detection methods.**[3]** Therefore, it can be applied to in biomedical, industry, and military application as shown in Fig.1-2.

Depending on the different transducing principles, the biosensors can be categorized to different types: resonant biosensors, optical-detection biosensors, thermal-detection biosensors, ion-sensitive field-effect transistor (ISFET) biosensors, and electrochemical biosensors. The electrochemical biosensors, based on the parameter measured, can be further classified as conductimetric, amperometric, and potentiometric. In this project, we focus on one type of electrochemistry biosensor, which measures the open circuit potential (OCP) to quantify the concentration of the analyte.

For electrochemical biosensors, it consists of analyte, transducer, and signal analysis and display part. The basic elements of electrochemical biosensor are shown in Fig. 1-3. Different analytes, obtained from various samples, such as cell culture media, human fluids (blood, urine, saliva), can be coupled to electrical interfaces through physical adsorption to create electrical signals that can be measured by the device. Ultimately, the electrical signal change, such as potential or current change can be monitored. Through amplification and analysis, the sensing signal is converted to concentration information for user use.

1.2 Introduction of molecular imprinting

Molecular imprinting technique is the process involves template-induced formation of specific recognition sites, followed by the removal of template to leave cavities which are complementary with the template molecules in the shape, size and steric configuration. [4] It has the following features. (1) Conformation reservation: The molecular imprinting process is supposed to "memorize" the features of template molecules; (2) Recognition specificity: After removal of the template, the cavity, which is complementary to the template molecules, can be well prepared, similar to the antigen-antibody interaction; (3) Reusability: low cost and high stability. [4-7] All of those features make molecular imprinting technical as an excellent method for analyte detection.

The main advantages of molecularly imprinted polymers (MIPs) are their high selectivity and affinity for the target molecule used in the imprinting procedure. A great number of small molecules have been imprinted successfully.[8] The best molecular imprinting performances have been obtained for molecules with molecular weights in the range of 200–1200 Da. However, expanding the technical toward recognition of macromolecules, such as proteins, DNA, viruses and bacteria appears to be extremely challenging. Bolisay et al designed a tobacco mosaic virus detection system through cross-linked polymers, which is able to distinguish tobacco mosaic virus easily. [5] TMV-imprinted hydrogels exhibited increased binding to Tobacco necrosis virus (TNV), while non-imprinted hydrogels bound similar amounts of TMV or TNV. In David W. Britt's review paper, they summarized a lot of examples on molecular imprinting on macromolecule, like hemoglobin, bovine serum albumin. [5]There are still have some difficulty for template removal because of those polymerization process. [7] Ou et al compared multiple different methods to remove template polymer. Lysozyme was molecular imprinted by polyacrylamide system, where the amount of lysozyme template able to be extracted was increased by the addition of methacrylic acid. [9]Therefore, an easy removal method of molecular imprint method is better for biosensor application.

Among the multiple types of molecular imprinting technical, self-assembled monolayers (SAMs), is particularly suitable for macromolecules imprinting. First, the process of SAM formation and chemical binding with the metal substrate is very easy; second, the high degree of

order and dense packing of long chains of the SAM provide a stable matrix for biosensor application. Tabushi and coworkers first applied the imprinting technique with SAMs for molecular recognition purpose.[10] (Tabushi et al., 1987). Zhou et al. built the chemical sensor by imprinting the target molecules in the ODS SAM on an indium–tin oxide (ITO) electrode and demonstrated successful detection for chiral amino acid, methylphosphonic acid, and dipicolinic acid [11, 12]. Hence, SAM could be a great platform for molecular imprinting of macromolecules.

1.3 Outline of Chapters

In Chapter 2, we applied MI biosensor to quantitative detection of carcinoembryonic antigen (CEA). Different techniques were applied to study the surface analyte absorption, and the molecular imprinting condition was optimized for the best performance of the MI biosensor. In the end, the MI biosensor was used to measure the CEA concentration in cyst fluid samples from 18 patients. The result obtained through the MI biosensor is consistent with ELISA results, which shows the potential application of MI biosensor for clinical detection.

In Chapter 3, the MI biosensor was further applied to a broad scale of analytes, ranging from a 3.5 nm protein to a 2 μm bacteria. The surface with multi-scale roughness was fabricated using the smooth and rough sides of a silicon wafer substrate. Through the experiment, we proved the capability of extending this biosensor to different types of macromolecules. In addition, we imprinted hemoglobin to fabricate a hemoglobin biosensor. The sensitivity as well as specificity of the hemoglobin biosensor was evaluated and the limit of the MI biosensor was investigated using a hemoglobin pH cross test. Through the pH cross test, the capability of differentiating subtle conformational differences was well proven.

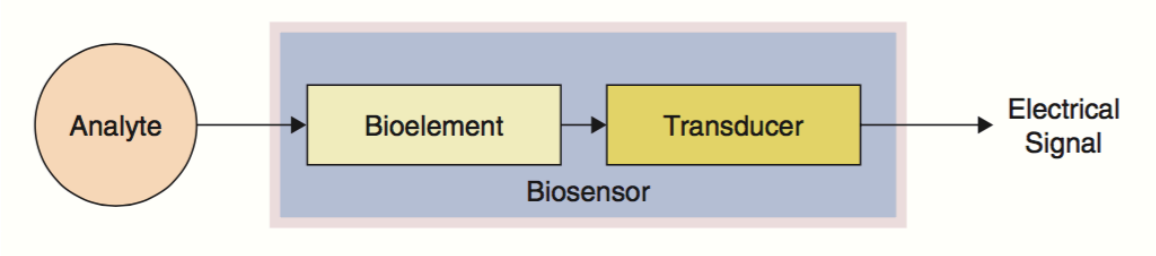

Figure 1-1. Basic set up of biosensor

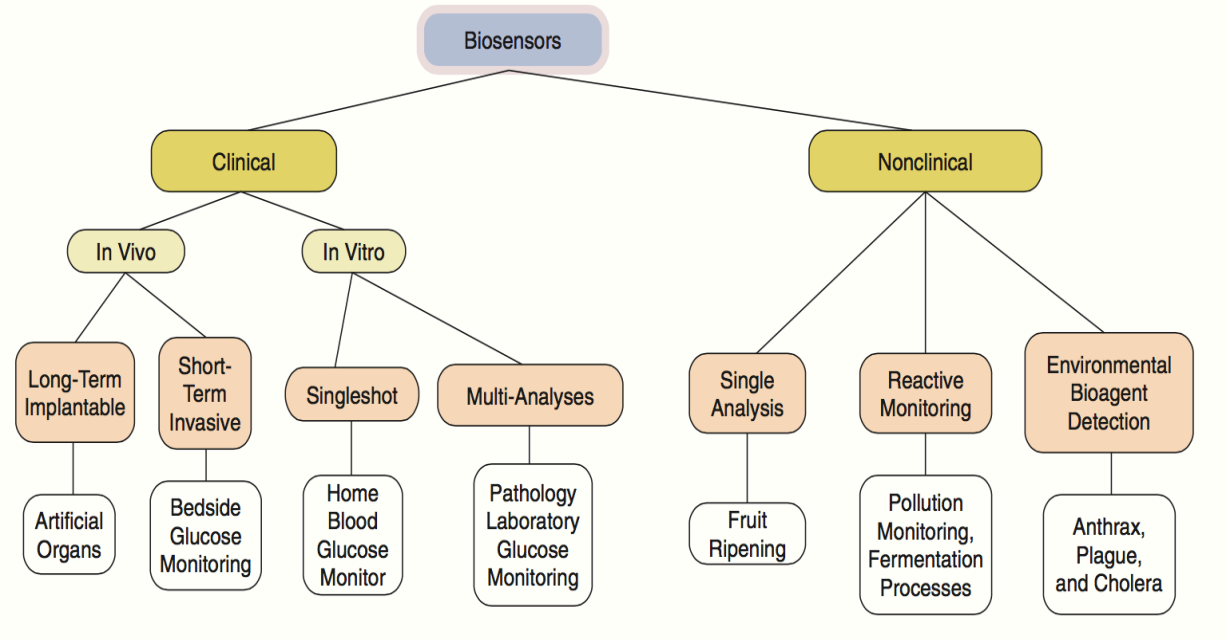

Figure 1-2. Potential application of biosensor

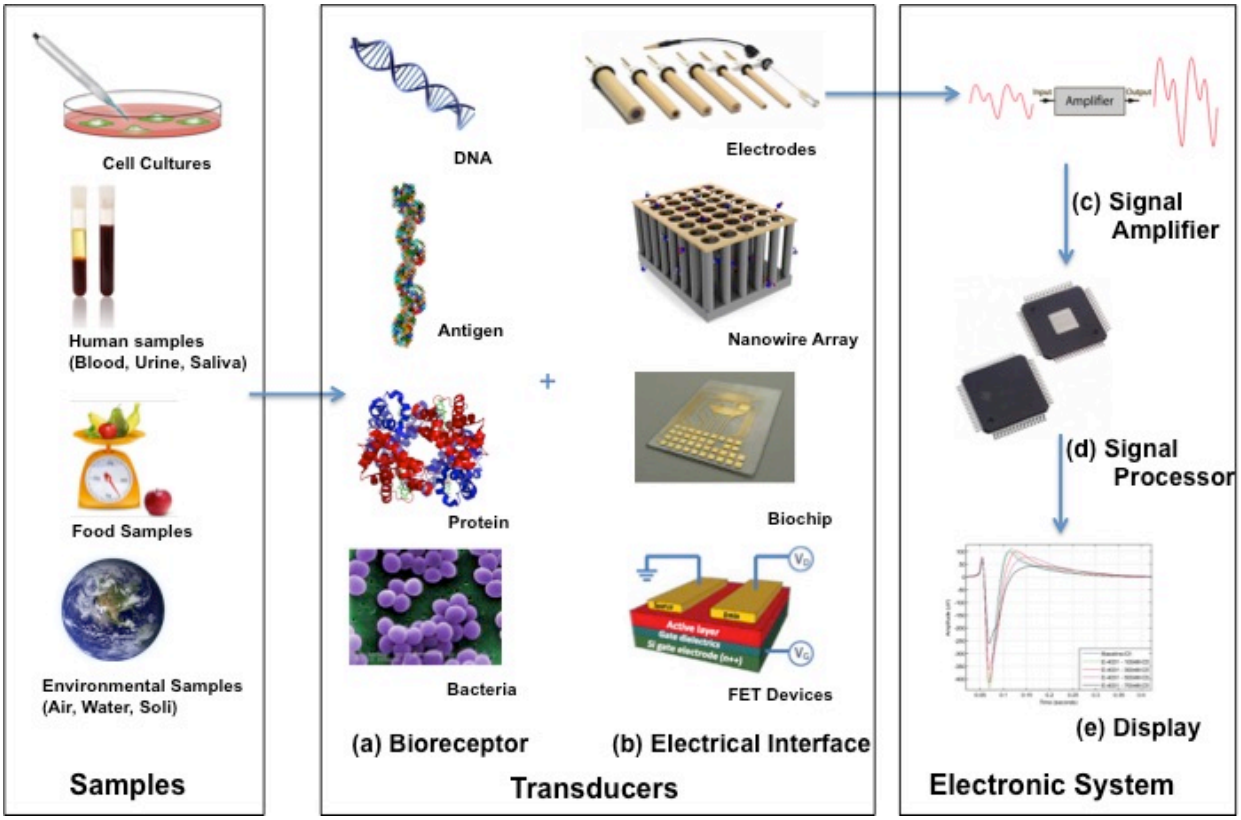

Figure 1-3. Elements of electrochemical biosensor

Chapter 2 Quantitative real-time detection of carcinoembryonic antigen (CEA) from pancreatic cyst fluid using 3-D surface molecular imprinting

2.1 Introduction

Pancreatic cystic neoplasms represent precursors to pancreatic cancer. Mucinous pancreatic cysts are most likely to undergo malignant transformation, rather than non-mucinous pancreatic cysts; and therefore early detection and management of these cysts is critical [13]. Carcinoembryonic antigen (CEA) is a glycoprotein, which can be easily found in mucosal cells that line the walls of pancreatic cysts[14, 15]. CEA production is greatest in mucinous pancreatic cystic lesions, and thus used to help differentiate high-risk pancreatic cysts from those with low malignant potential. Currently, the most common detection method for CEA is the enzyme-linked immunosorbent assay (ELISA), which is widely used for clinical detection. This method is fairly complex and takes at least ten hours to complete a series of steps leading to the final immunofloroscent staining. Furthermore, the equipment required is fairly sophisticated and not available in most hospitals. Consequently it may take several days to weeks to obtain the results. Pancreatic cysts are frequently observed inadvertently during other procedures and having an immediate analysis of their CEA content is critical in order to determine further course of action. Here we show that the potentiometric method can provide rapid, selective, sensing whose accuracy is similar to ELISA, but which requires one tenth of the fluid volume and obtain results within 20 minutes or less. The technique, based on a modified three dimensional self assembled monolayer (SAM) imprinting method, is robust, simple to implement, portable, inexpensive, and can be made readily available in the operating room or in any hospital or clinic.

The use of SAMs for surface molecular imprinting of potentiometric sensor was first reported by Yanxiu et al [12, 16-21] . They used octadecyltrichlorosilane (OTS) to imprint simple amino acids on ITO glass, where they demonstrated that potentiometric detection was sufficiently sensitive not only to discriminate between different amino acids, but it could also discriminate between amino acids of similar structure, but different chirality. Despite the promising results, this method had several drawbacks that prevented its implementation for the detection of more complex biological molecules. First, OTS is hydrophobic and is suspended only in non-polar solvents, which makes if difficult to imprint most biological molecules that are

hydrophilic. Second, OTS reacts only with Si oxides, where the sensors used were imprinted mostly on flat ITO substrate. This limited their use to small molecules, whose radii were smaller than the thickness of the SAM, or at most 1.2 nm [22-25]. We show that these obstacles can be overcome if; (a) The SAM is coated on Au which is evaporated onto Si rather than coating the SAM directly on the bare Si surface which is atomically flat (RMS roughness ~0.6 nm). In contrast to Si, which is a single crystal surface, evaporated or sputtered Au films form microcrystalls and have an RMS roughness of 3-4 nm, which is similar to the dimensions of most protein molecules. This allows the proteins to be enveloped by the templating SAM and enables three-dimensional imprinting. The latter greatly increases the accuracy of detection and the limiting size of the molecule being detected [26]. (b) A far larger range of SAMs with different functionalities is available when thiol rather than trichlorosilane chemistry is used. Thiols, which are end functionalized with OH groups, are hydrophilic and can be suspended together with a much large range of biological molecules, such as enzymes, viruses, bacteria, and proteins. Wang et al [27] demonstrated the ability of this technique to detect and differentiate between polio and adenoviruses, as well as between other proteins such as hemoglobin and myoglobin [26]. Yet, despite its promise, the method had not been applied "in vivo" to actual physiological fluids, where its sensitivity and selectivity could be probed in the presence of multiple other factors present in bodily fluids and where the results could also be verified using standard methods in an independent pathology laboratory.

In this paper we probe the clinical relevance of the potentiometric method by using it to evaluate the CEA concentration in pancreatic cyst fluid obtained from 18 patients, under IRB 95867-6. We chose CEA, as our probe, due to its availability in highly purified form and its physiological importance as a marker for colon, breast, and pancreatic cancers. We used the potentiometric sensing to measure the amount of CEA present in wet biopsies taken from the pancreatic cysts and then compared the results with those obtained using ELISA from the hospital pathology laboratory. Excellent agreement between two methods proves the accuracy of molecular imprinting biosensor.

2.2 Materials and method

2.2.1 Materials

11-mercapto-1-undecanol (SH-$(CH_2)_{11}$-OH), dimethyl sulfoxide (DMSO), potassium ferricyanide $K_3[Fe(CN)_6]$, potassium ferrocyanide ($K_4[Fe(CN)_6]$, CEA from human fluid, human CEA ELISA kit were all purchased from Sigma Aldrich, matrix metalloproteinase-7 (MMP-7) , gold/chromium (100nm/10nm) coated on silicon wafer substrate fabricated in the Cornell NanoScale Facility, Dulbecco's Phosphate-Buffered Saline (DPBS) buffer was used as detection solution for all the tests.

2.2.2 Biosensor fabrication

Gold/chromium (100 nm/10 nm) coatings on single crystal [1,0,0] silicon wafers were prepared using electron beam evaporation at a vacuum of 10^{-7} Torr in the Cornell NanoScale Facility. The chromium layer here was to improve the adhesion of the gold to silicon. The gold-coated substrate (1.5 cm × 2 cm) was rinsed with ethanol and dried under nitrogen gas before use. In order to keep the working area of each gold substrate constant, the teflon tape with an 1.26 cm diameter hole made by a hole puncher is adhered to the gold surface. Thiol/DMSO and protein/DI water blend solution with proper ratio were prepared as imprinting solution to make well-ordered SAM on gold surface. Thiol and protein mixture were made as follows: the template molecules (CEA) were dissolved in de-ionized water and the alkanethiols, were dissolved in DMSO. The two solutions were then mixed at 19:1 (V: V) respectively to make 100 uM final thiol concentration. The prepared gold-coated chip was immersed into blend solution at room temperature for 2.5 hours and soak into 1 M NaCl aqueous solution for 1 hour to remove the template molecules.

2.2.3 Pancreatic cyst fluid sample preparation

Patients presenting to Stony Brook hospital's endoscopy unit for pancreatic cyst evaluation by means of endoscopic ultrasound (EUS) were enrolled for study. As standard of care at the time of this study, EUS-guided fine needle aspiration (FNA) is performed of all pancreatic cysts greater than 1-2 cm in size, or those lesions with high-risk morphological features under ultrasound. The endoscopic technique of EUS-FNA has been previously described [13]. Fluid is aspirated from the cyst cavity using a through-the-scope 25 gauge or 22 gauge FNA needle. The fluid is examined for cytological content and morphology, as well as the level of amylase and CEA by the means of ELISA. For the study purposes, an additional 0.5 ml of

pancreatic cyst fluid was collected and immediately centrifuged in order to separate cyst fluid content from red blood cells.

2.3 Results and discussion

2.3.1 Model of the CEA molecular imprinting process

The basic molecular imprinting mechanism is illustrated in Figure 2-1. CEA, as the analyte in this study, can be viewed as a rod shaped molecule with 8 nm diameter and 23 nm length. [14]. CEA molecules are adsorbed simultaneously with the thiol molecules onto the gold-coated Si chip to form a self-assembled monolayer. The new mechanism for molecular imprinting, differs from the one previously proposed, where it was assumed that the thiols were adsorbed together with the analyte on an atomically flat surface where a monolayer was formed around the analyte. In that model the templating was determined only by the size of the thiol chain, which was a maximum of 2 nm [26]. This model worked well when the templating was performed on atomically flat surfaces, such as those of native oxide covered Si and the analytes were small molecules, such as methylphosphonic acid (MPA)[28]. Hence it was very difficult to explain how imprinting with protein larger than 10 nm which are nearly ten times larger than the thiol molecule, could achieve molecular imprinted sensors with selectivity that could discriminate between hemoglobin and myoglobin, as previously reported [26, 27]. Based on the results in this manuscript, we propose an alternate quasi-3D molecular imprinting model as shown in Fig. 2-1 B. In contrast to native oxide coated Si, physical vapor deposition (PVD) of gold substrate results in films with surface roughness having RMS ~ 3-4 nm, as shown in the AFM scan in Fig. 2-1A. The co-adsorption process of thiols and proteins on these surfaces is illustrated in step b in Fig. 2-1 B. The thiols adsorb to the gold surface and form a closely packed crystalline layer, which, as shown in side view of Fig. 2-1 B, is conformal to the morphology of the gold surface. During the co-adsorption process, CEA fits into one of the crevices formed on the gold surface. The thiol molecules, which are adsorbed at the same time, fill in the spaces "fitting" the CEA molecule accurately into the space provided through hydroxyl group or hydrophobic force between the thiol and template protein. The imprinting molecules are then removed by soaking the chip in 1 M NaCl for one hour, leaving behind the very specific three dimensional cavity imprint as shown in Fig. 2-1 B step c. When the sensor is next exposed to the

detection solution, only the molecules fitting precisely into the three-dimensional imprinting pattern can fit and trigger the potential response.

Each step of molecular imprinting process on the gold surface was monitored through CV and EIS [16, 29]. CV was employed here to investigate the effect of adsorbed thiol and protein layer on electron transfer between the gold electrode and an electroactive moiety in solution, namely, $K_3Fe(CN)_6$. In Fig 2-3(A), before imprinting, conductive bare gold surface facilitate electron transport, and producing an apparent pair of reversible $Fe(CN)_6^{4-/3-}$ redox peaks at E_{pc} of 0.321V and E_{pa} of 0.167V. After imprinting, the anodic and cathodic peaks disappeared which result from a decrease in the electron transfer rate constant due to the gold electrode surface becoming coated with a condensed non-conductive thiol/CEA layer. This layer act as a barrier, which prevents the ferricyanide ions from approaching the electrode surface. To further remove the template CEA molecules, the imprinted electrode was soaked in 1M NaCl for one hour, which is the optimal method selected to remove the CEA templating molecules. The redox peaks re-appear, suggesting the successful removal of the CEA template and increasing the area exposed on the gold surface. Finally, upon the addition of 8.5 ng/mL CEA to the solution, the redox current was again reduced by a factor of 0.4, with Epc and Epa shifted to 0.314V and 0.125V, which suggested an efficient recognition of CEA by a large faction of the cavities and a partial occupation of those by the CEA molecules.

In the EIS experiment (Fig. 2-3 B), bare gold substrate displayed a straight line, corresponding to a mass diffusion-limited electron transfer process. After the co-deposition of thiols and CEA, the straight line was converted to a well-defined semicircle, characteristic of the largely increased electron transfer resistance, R_{et}. The subsequent removal of CEA templates by 1M NaCl changed the semicircle back to a straight line, indicating the exposed gold surface in the MIP cavities, when the re-addition of CEA would increase R_{et} again due to the reoccupation of the cavities by CEA. This trend nicely agrees with which we observed with CV and clarifies the working mechanism of CEA MI biosensor as illustrated in Fig. 3-1.

2.3.2 Estimation of CEA absorption on gold surface

In order to optimize the imprinting process we first determined the adsorption isotherm of CEA onto the gold surfaces. Solutions of CEA in concentrations of 5, 10, 15, 20 ng/ml were prepared in DI water, and in blend thiol/CEA imprinting solution respectively. Cleaned bare gold

chips with same working area were immersed into either CEA/DI or CEA/Thiol/DI blend solutions for 2 hours to let the CEA molecules absorb fully to gold surface. After the absorption process reached equilibrium, the amount of CEA remaining in solution, R, was measured using ELISA. The results are shown in the inset to Figure 2-3 (A), where we plot the original amount of CEA mass in the solution, R, vs the mass of CEA adsorbed on the gold surface, or (1-R). From the figure we can see that below 100 ng of CEA imprinting mass the two curves are nearly identical, where the adsorbed concentration increases linearly with the total CEA mass in solution. Above this concentration, the solution in DI increase with a slightly smaller step, while the solution containing thiol saturates, due to the thiol molecules competing for the surface area on gold with CEA molecules.

2.3.3 Optimizing the OCP response vs CEA concentration curve

In order to achieve the largest OCP response signal for CEA addition, the surface molecular imprinting condition has to be optimized. In Figure 2-3 (A) we plot the OCP change of the CEA biosensor as a function of CEA addition in testing medium. CEA sensors were fabricated in 4 different CEA imprinting concentrations, 5, 10, 15, and 20 ng/ml. The CEA sensor OCP response curves for each condition are plotted in Fig.2-3 (B). The typical OCP response of the CEA potentiometric sensor curve composed of a linear region where the OCP change is directly proportional to the analyte CEA concentration in testing medium. This region is followed by an abrupt transition to a plateau region, where the OCP response remains fairly constant despite increasing analyte concentration.

In the linear region, the imprinted cavities are being filled by the analyte CEA molecules, where the OCP change gradually increases due to the electron current generated by the number of cavities filled by CEA. The linearity of the OCP change is an indication that minimal overlap occurs in filling the imprinted cavities. Once all the cavities are filled, the OCP response is kept the constant with the increasing of CEA addition, as the gold surface saturation occurs at this CEA imprinting concentration.

The dynamic range of CEA biosensors also increased with the imprinting concentration of CEA. The widest dynamic range, from 0 to 8.5 ng/ml, can be obtained at CEA imprinting mass of 15 ng/ml. Once all the cavities are filled, the OCP response no longer increases since the gold surface is now fully covered by CEA and/or thiol molecules. The slope of the OCP response

and the CEA concentration curve in the linear region determines the sensitivity of the biosensor. The larger the slope of the linear region and the higher the maximum value, the more sensitive and wider the dynamic range of the biosensor. A clear maximum response occurs at 15 ng/ml. The slopes of the curves at 15 and 20 ng/ml are nearly the same, but the linear range at 15 ng/ml is wider, indicating that overlap of the imprinted areas begins to occur at higher concentrations. From the optimization curve, both the maximum OCP response and the slope increase with CEA imprinting concentration until 15 ng/ml, suggesting the largest number of cavities created at 15 ng/ml CEA imprinting condition. Therefore, 15 ng/ml CEA concentration is the optimal imprinting condition to generate the largest OCP response for the CEA biosensor.

The formation of cavities by the imprinting method can be confirmed by titrating the gold surface after removal of the imprinted CEA molecules. It is well established that thiol molecules are adsorbed to the gold surface through strong sulfur-Au bond to form self assembled monolayers (SAMs) via the electron transfer reaction [19, 21], R-S-H + Au -> R-S-Au + e^- + H^+. Therefore the adsorption process could be studied by observing the OCP generated during the thiolation process, which could provide a qualitative confirmation of the exposed gold area created by washing off the imprinted CEA. In order to determine the OCP generated to fully cover the bare gold electrode, a thiol/DMSO solution with concentration of 0.4 mg/ml was prepared and gradually added into the testing solution. The curves are shown in Figure 2-3 (C), a plateau value of 120 mV is obtained at a titration concentration of 70 uM for thiol titration on bare gold surface, corresponding to the maximum coverage of the exposed free gold area on the gold surface. However, when we titrated same thiol solution to a well-incubated 100 uM thiol layer, no obvious OCP response is observed due to the insulating thiol layer block the electron transfer during thiolation process. The other curves shown in Fig. 2-3 (B) correspond to titration of electrodes, which had been imprinted with different CEA concentrations, and then removed the template CEA. The OCP response on these curves is assumed to increase with thiol concentration till the exposed areas are fully covered, which means a dense insulating SAM layer formed on the gold surface. From the thiol titration process, the largest number of CEA imprinting cavities formed at the 15 ng/ml CEA imprinting condition, which confirms the CEA optimal imprinting as shown in Fig. 2-3 (A). The side view of the process for each curve is compared schematically in Fig 2-3 (C) where arrows point to selected curves corresponding to the illustrations. At the two extremes, the bare gold surface corresponds to the blank gold surface

without SAM formation, while the one exposed to the100 uM thiol solution corresponds to the surface fully covered with an SAM. The curves in between correspond to the geometry where bare gold areas become exposed within the SAM after the imprinting CEA molecules are removed. This model is further confirmed using CV (shown in the inset), where a large redox peak is observed on the bare gold surface. Exposure of the electrode to 50 μM thiol solution produces partial coverage and reduces the redox peak, while exposure to 100 μM solution nearly eliminates the signal, consistent with formation of an insulating SAM.

We can estimate the number of CEA molecules that participated in forming the imprinted region on the electrode from the CEA mass at the saturation point of the response curve. This value represents the maximum amount of CEA molecules required to fit into the cavities of CEA biosensor. In the linear regime, each CEA molecule contributes the same amount of charge, and hence the potential increases linearly with concentration. Once all the exposed Au surfaces are filled, other molecules are adsorbed on the thiol layer, and generate far less charge. The concentration of CEA at the intersection of the linear and plateau regions corresponds to the mass of CEA or the number of molecules required to fill all the voids left by the imprinting process. The results are plotted in Fig 2-3 (A) as a function of the CEA imprinting concentration, where we can see that the mass of CEA which is available for detection is smaller than mass of the CEA adsorbed onto the Au during the imprinting process.

2.3.4 Re-usability, stability, and storage of MI biosensor

The good agreement between the ELISA and titration results also raises the question as to how many times can adsorbed CEA be removed form the imprinted regions, i.e. how many times can the imprinted sensor be washed and re-used before degradation in performance occurs?

In Fig. 2-4 (A) we show the OCP response curves obtained from a chip imprinted at a optimal CEA imprinting concentration of 15 ng/ml after the first use, followed by soaking in 1M NaCl for one hour to remove imprinted CEA, and exposing again to the detection solution to follow the same CEA measurement procedure as before. From the Figure 2-4 (A) we can see that small degradation occurs after the first two uses. Using the same chip a third time though shows obvious deterioration. The slope of the OCP response curve did not decrease a lot, but the saturation concentration decreased from 8.5 ng/ml to 4 ng/ml. This decrease dues to means after

3 detection-washing cycle of CEA molecule into the cavity of the sensor, the quality of the SAM decreased, result in the shrink of the dynamic range of the CEA sensor. In the inset of Figure 4A, the OCP response of the sensor gradually decreased with the increasing use cycles, and ultimately disappeared after the fourth attempt.

Stability can also be measured by determining the length of time that the chip can be used without degradation after the imprinting occurred. Chips were imprinted with CEA at 15 ng/ml and tested with analyte immediately or after 24, 48 or 72 hours. Three methods of storage were used during these periods, desiccator (100 Torr), ambient air, and submerged in DI water. According to the results, shown in Figure 2-4 (B), when stored in a desiccator, minimal degradation occured up to 48 hours and only partial degradation was observed after 72 hours. Storage in DI water incurred a 50% decrease in potentiometric sensitivity within the first 24 hours, while storage in ambient conditions resulted in a loss of nearly 70% within the first 24 hours. CV of the surfaces obtained after 72 hours indicated that the surfaces were still fully covered with thiols. Hence no displacement of thiols occurred either in water or air, as expected given the strength of the gold-sulfur bond. The large difference between the samples stored in vacuum vs those stored in air or water indicated that the most probable mechanism for the decrease in performance was due to surface contamination of the hydroxyl groups .

2.3.5 Calibration and selectivity test of CEA MI biosensor

In order to obtain absolute readings of the CEA concentration and compare them to those obtained using ELISA analysis, a two-step calibration process was followed. First, the potentiometric response obtained from the biosensor was calibrated against aliquots of known concentration. The results shown are Figure 2-5 (A) where the response function is observed to have two distinct regions, a linear section and a plateau region. The OCP response corresponding to a given analyte concentration in the test solution can be obtained by fitting the linear region, as shown in Figure 2-5 (B).

Second, samples of known CEA concentration were analyzed using both ELISA and the biosensor. The values obtained form the biosensor output were plotted vs those obtained with the ELISA reader in Figure 5C. From the figure we can see that eventhough the he data are well fit be a linear relation ($R^2 = 0.98$), the ELISA readings were consistently larger by 9%.

The selectivity of the biosensor imprinted for CEA was further confirmed by cross testing with MMP 7, another common tumor marker. In Figure 2-5 (A), we find that no OCP response is observed in the absence of CEA.

2.3.6 Usage under physiological conditions

Patients presenting to Stony Brook hospital's endoscopy unit for pancreatic cyst evaluation by means of endoscopic ultrasound (EUS) were enrolled for study (IRB#95867-6). As standard of care at the time of this study, EUS-guided fine needle aspiration (FNA) was performed of all pancreatic cysts greater than 1-2 cm in size, or those lesions with high-risk morphological features previously observed under ultrasound. The endoscopic technique of EUS-FNA has been previously described [13]. Fluid was aspirated from the cyst cavity using a through-the-scope 25 gauge or 22 gauge FNA needle. The fluid was then sent to the hospital pathology laboratory where it was analyzed for cytological content and morphology, as well as the level of amylase and CEA by the means of ELISA. An additional 0.5 ml of pancreatic cyst fluid was collected for study purposes which was immediately centrifuged in order to separate cyst fluid content from red blood cells, and stored in a freezer at –80 degrees. The CEA content of the cyst fluid was determined by thawing the samples and adding 10 microliters of cyst fluid into a total volume of 10ml of PBS. The solution was further diluted till the OCP reading was in the linear range of the sensor. A set of sensors was fabricated according the protocols described previously. Two readings from two different imprinted sensors were taken from each patient. The CEA concentration was determined from the OCP response using the calibration curve established above and correcting for the ELISA offset. The average values and corresponding standard deviations are plotted in Figure 6. From the figure we can see that the concentration ranged over three orders of magnitude, where the highest readings were obtained from patients diagnosed with adenocarcinoma. From the figure we can see that the data can be fitted with a straight line, having a slope 1.011 (95% confidence interval M= 0.9943 to 1.028, Chi^2=0.9157). In order to ensure that the fitting parameters were indeed consistent over the entire range, the low concentration region, outlined in the red box of the figure was fit separately as well and is plotted in the inset of Figure 2-6. The slope obtained, 1.016 is not significantly different than that obtained over the whole range, 1.011. These results indicate that the response of the sensor is

highly linear over a very large concentration range and the calibration procedure relative to the ELISA method outlined above is accurate and reproducible (n>40 trials). Furthermore, the accuracy of the results is comparable to that obtained with ELISA, yet the volume of fluid used ranged from a maximum of one hundred microliter at the lowest concentrations to 10 microliters in the cancerous cysts, as compared to a volume of at least 150 microliters required for the ELISA test. In addition, the results were obtained in 5 minutes, as opposed to a minimum of 10 hours, required by the ELISA test. Hence the accuracy and the analysis time for this sensor are ideal for use at bedside and can allow the physician to make an informed decision regarding the potential malignancy of the cyst. In case the cyst is malignant or simply to minimize the disturbance of the cyst the smaller volume required for analysis is a distinct advantage.

Finally, these results also indicate that the biosensor was able to maintain its selectivity for CEA despite the presence of many other proteins and markers in the cyst fluid. Despite the accuracy of the sensor in detecting a single analyte, confidence in the determination of malignancy requires simultaneous detection of multiple analytes. These results confirm that this can be accomplished by combining several sensors, imprinted for different markers, whose response can be multiplexed and recorded separately as part of a chip based sensing array.

2.4 Conclusion

In conclusion we have shown that a potentiometric sensor can be constructed whose accuracy for the detection of CEA in pancreatic cyst fluid obtained from 18 patients is comparable to that obtained by ELISA over a concentration range spanning nearly three orders of magnitude. We also showed that this sensor could be used at bedside since the measurement required only 1% of the volume needed for the ELISA determination and the results were obtained within 5 minutes using a portable potentiometric analyzer. Hence this sensor can allow the physician to make a rapid diagnosis as to further treatment of cysts which were discovered incidentally during other procedure.

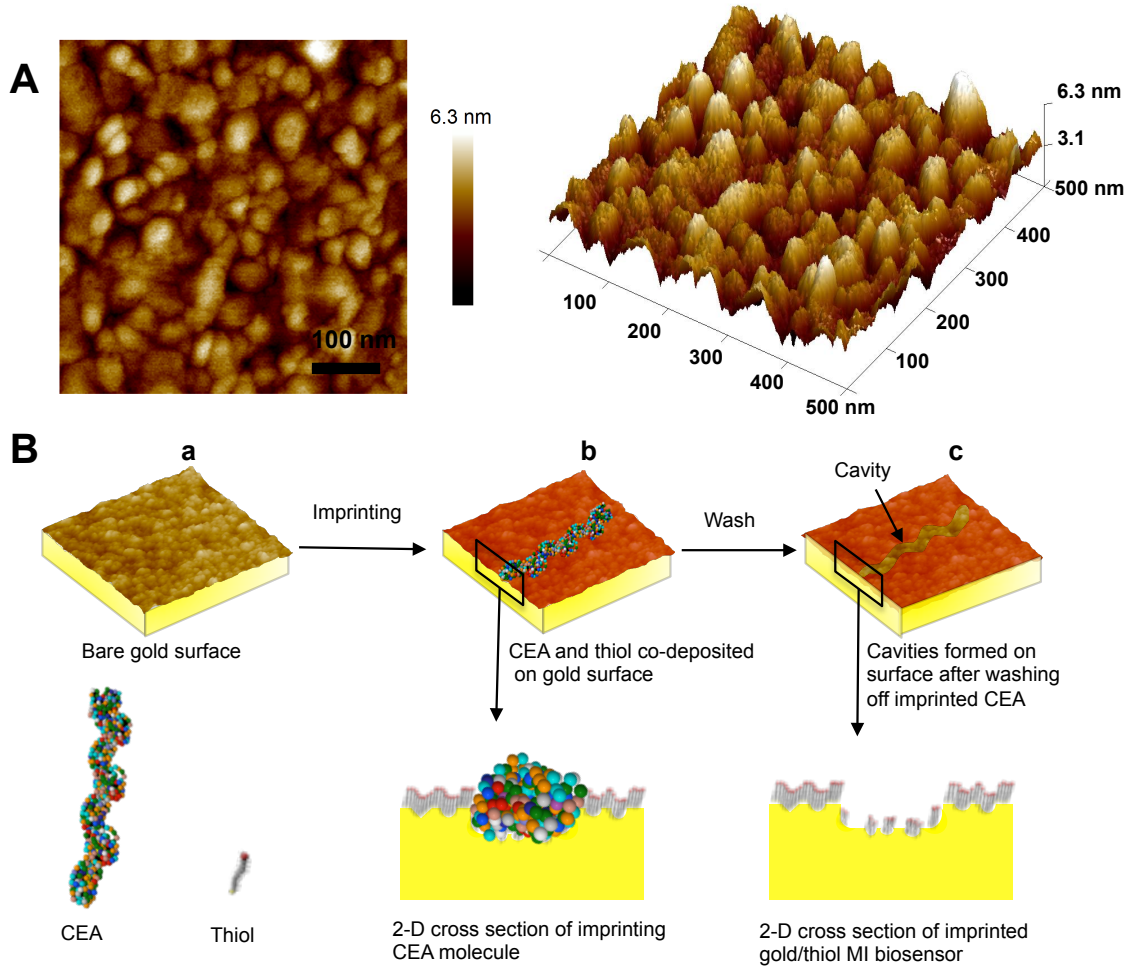

Figure 2-1. (A) 2D and 3D AFM image of bare gold. (B) Schematic of the molecular imprinting process. (a) Bare gold, before imprinting. (b) Thiol coated gold surface with adsorbed CEA molecule after imprinting, red color layer represents SAM coverage and (c) The footprint of the CEA molecule created in the SAM layer after it is removed by washing. The cartoon below the figure shows the process in a cross-sectional view.

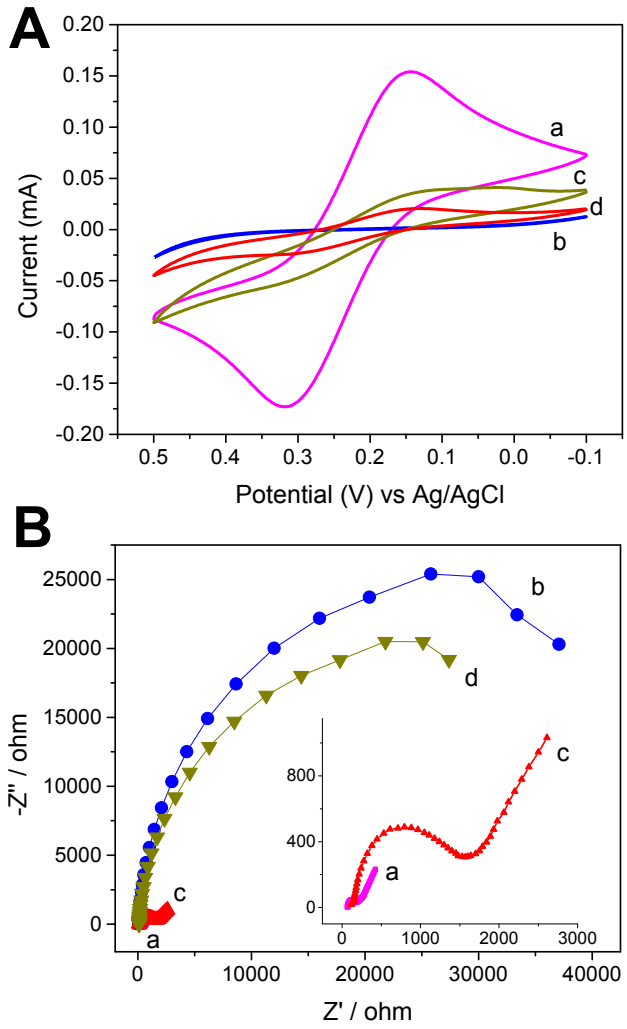

Figure 2-2. (A) Cyclic voltammograms (CV) of the different electrodes (a) bare gold, (b) after CEA imprint, (c) after washing, (d) after addition of CEA (8ng/ml): Scan rate, 0.1 V/s. (B) Electrochemical impedance spectra (EIS) of different electrodes: (a) bare gold, (b) after CEA imprint, (c) after washing, (d) after addition of CEA (8ng/ml). Inset: EIS of (a) bare gold (c) and after washing. EIS was tested with 5 mV amplitude and frequency range of 0.1-100,000 Hz. Both CV and EIS were performed in KCl solution (0.1M) contanining $Fe(CN)_6^{3-/4-}$ (5 mM).

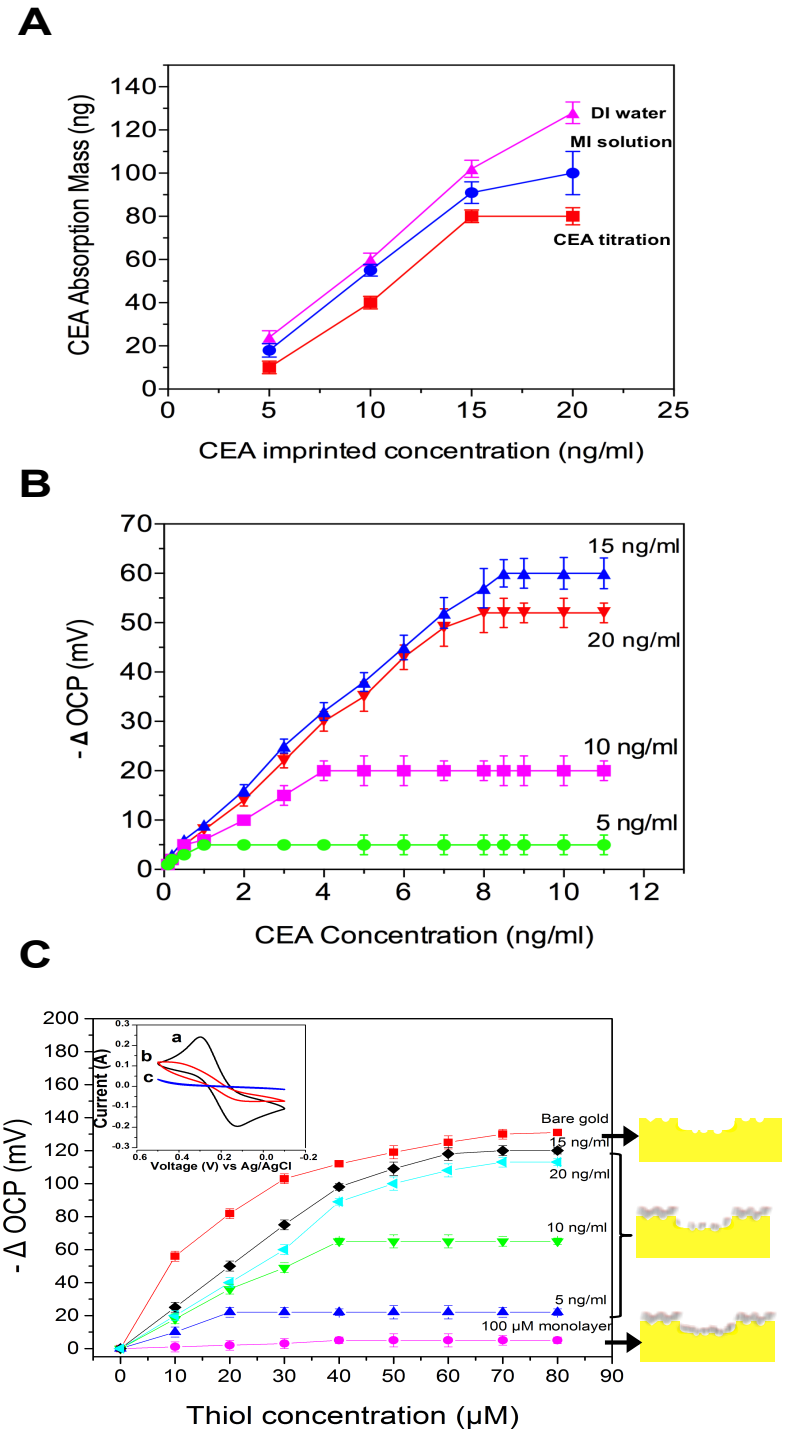

Figure 2-3. (A) OCP response of the electrodes imprinted at four different CEA concentrations, as shown in the figure legend. Note all curves have a linear and a plateau region. Inset: Maximum OCP at the intersection of the linear and plateau regions for different CEA imprinting concentrations. (B) Thiol titration: OCP response as a function of thiol concentration added into

testing solution on an imprinted gold electrode, as illustrated in the schematic adjacent to the figure. Inset: CV of bare gold and SAM. (C) The amount of adsorbed CEA mass as a function of the CEA concentration in the imprinting solution, as measured directly via ELISA or inferred from the titration experiments with thiols or CEA molecules.

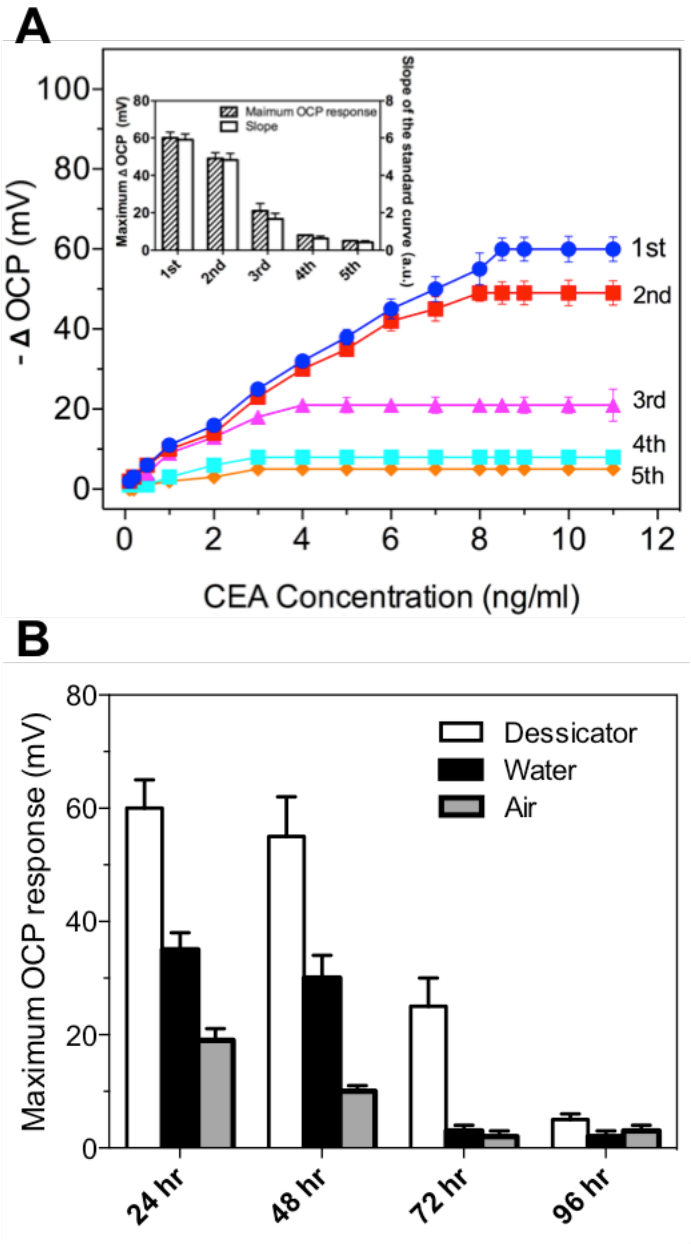

Figure 2-4. Stability testing of the molecular imprinted biosensor: (A) OCP response of a CEA molecular imprinted biosensor after multiple repetitions of the detection/wash cycle. In set: Maximum OCP response and slope of OCP response curve vs cycle number (B) The slope and maximum OCP response for CEA imprinted sensors after storage in a vacuum desiccator, DI water, and air for up to four days.

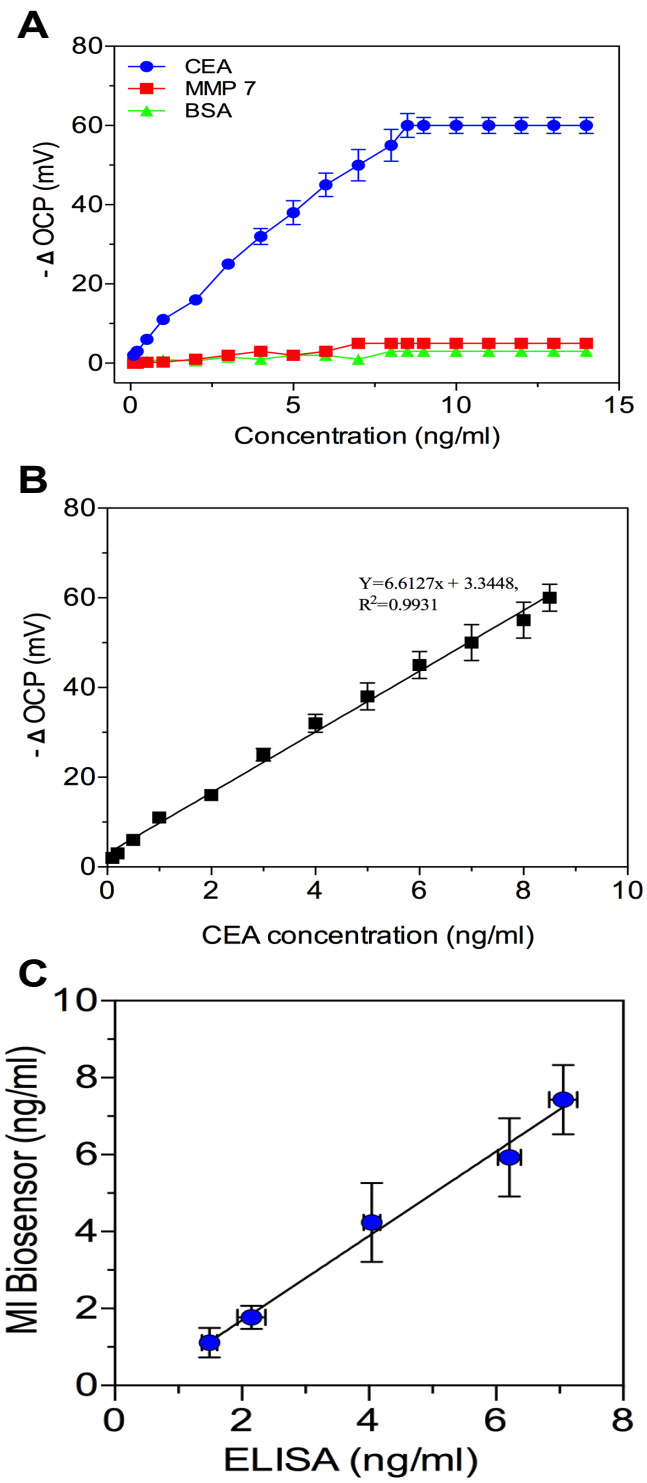

Figure 2-5. (A) CEA biosensor selectivity test: OCP response of the sensor imprinted with CEA and tested with MMP 7 respectively. Calibration of the CEA imprinted sensor: (B) OCP response of the biosensor after addition of CEA in the linear response region. (C) Calibration of

the CEA imprinted sensor: MI reading of known concentration of CEA vs ELISA reading of the concentration.

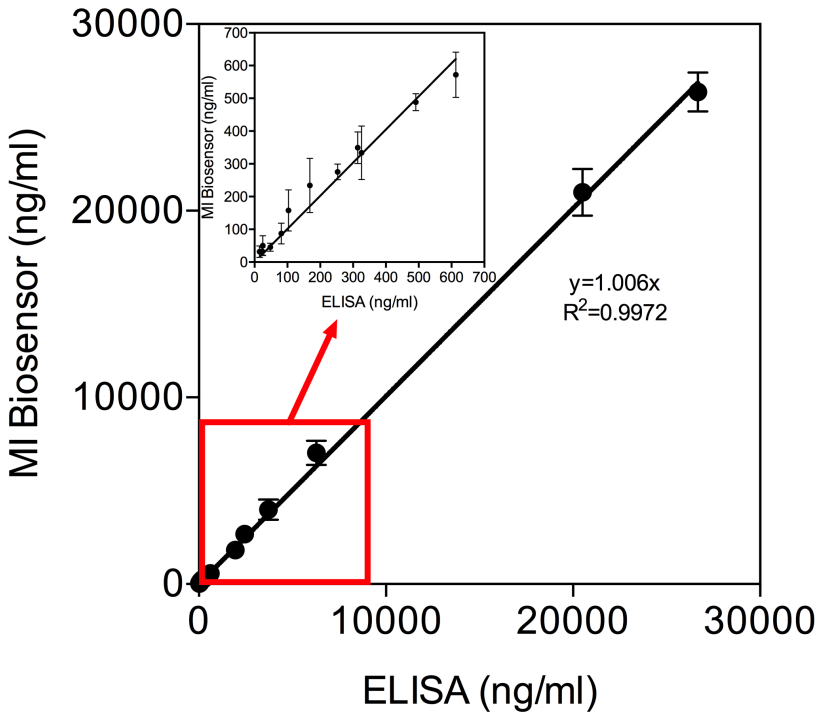

Figure 2-6. CEA concentrations in the pancreatic cyst fluid from 18 patients. The biosensor reading plotted vs the ELISA reading of the samples obtained from the official pathology report. Inset: Magnified section of the points near the origin.

Chapter 3 Design of molecular imprinting biosensor with multi-scale roughness for bio-molecular detection

3.1 Introduction

Electrochemical biosensing enables highly sensitive detection of analytes and transmission of data wirelessly to remote areas.[25, 30-46]They have the potential of being integrated into smart responsive biomedical systems, such as sequencing devices[47, 48], triggered drug delivery platforms and rapid pathogen sensors that report to medical personnel. Compared to the traditional immunohistochemistry, electrochemical sensors provide results quickly, are inexpensive and portable[32, 33, 49, 50]. In our previous study, electrochemical detection was presented as a strong alternative to conventional ELISA for protein biomarker quantification[25]. Moreover, DNA chips producing electrical signal have long been proposed[34, 43, 48, 50]. Recently, Miao et al pioneered ultrasensitive biosensors for microRNA as a crucial biomarker for diagnosis and prognosis of cancers[51-53]. In addition to clinical uses, electrochemical sensors have been widely applied in environmental monitoring. Multiple sensing approaches have been devised by Chen et al to quantify Escherichia coli and Staphylococcus aureus in drinking water[54, 55].

Herein, we present a potentiometric molecular imprinting (MI) technology that provides a real-time and label-free sensing interface to be integrated into the devices.[19, 44, 50, 56-59] Although there are tremendous researches about biosensor in the past two decades, most of them are only capable of detecting certain analyte based on their special property or relationship between analyte and the interface.[24, 25, 39, 43, 46, 49, 50, 54, 55, 57, 60-67]Designing a biosensor, which is applicable to a broad set of the biomolecules, can greatly improve the detection efficiency. Hence, molecular imprinting, based on the classic “lock and key” model, turns out to be a universal detection platform for application on various analyte[5, 6, 27, 63, 68]. With the unique structure and conformation of the biomolecules, different analytes, such as protein, antigen, virus, can be easily differentiated by MI biosensor.

The technique of surface molecular imprinting was first used octadecyltrichlorosilane (OTS) self assembled monolayers for imprinting amino acids on ITO electrodes[12]. This

technique could be so sensitive that it was able to not only differentiate between different molecules, but also determine their chirality. The drawbacks though were the fact that OTS is hydrophobic and the method is limited to analytes soluble in non-polar solvents. Furthermore, they showed that the technique was only able to sense molecules whose dimensions were similar to the OTS layer thickness, or 2 nm. Later, Wang et al showed that larger bio macromolecules, could also be detected if the imprinting SAM was made with hydrophilic moieties, such as -OH terminated thiols[5-7, 12, 26, 27, 39, 68-70]. In their study, entire proteins were detected rather than single small amino acids, which was inconsistent with the early predictions which postulated that the technique was limited to analytes not significantly larger than the thiol monolayer thickness[12]. We then postulated that the surface roughness of the imprinting electrode could also be a contributing factor in the molecular imprinting process. Therefore, that the dimension that limits the size of the imprinted analyte was not simply the SAM layer thickness, but rather the size of the analyte relative to the surface roughness. Hence, when the imprinting was done with OTS on a ITO glass whose surface roughness was 0.6 nm, the SAM layer thickness, of approx. 2 nm was the larger and hence the limiting dimension[12, 17-19, 21, 28, 71]. When imprinting was done with OH-terminated thiols assembled on gold coated Si electrodes, the RMS roughness of the gold which was much higher than the SAM layer, and dimensional limit of the analytes which could be detected was increased.

We therefore propose a 3D molecular imprinting model where the efficiency and sensitivity of the potentiometric biosensor could be enhanced even more if the surface roughness was tailored to match the size of the analyte molecule. In this model the surface morphology formed a niche which surrounded the analyte and the SAM formed a precise coating surrounding the analyte in three dimensions. In this manner one would be able to significantly increase the range of detectable analytes, and the versatility of the technique. In our previous study, a CEA biosensor based on MI was successfully designed, and applied to the detection in patient cyst fluid. The result obtained from MI biosensor is comparable to the result detected through ELISA, but required much less time. In this contribution, we designed the MI biosensor on multi-scale roughness surface, by matching the analyte size to the proper gold surface, this MI biosensor can be extend the to the detection of a much wider spectrum of biomolecules with different sizes ranging from a few nanometer proteins to hundreds of nanometer virus.

3.2 Materials and Method

3.2.1 Materials

The different analytes used for molecular imprinting are listed in Table 1. Carcinoembryonic antigen (CEA) from human, myoglobin (Mb) from equine skeletal muscle (Mw = 17.6 K Da), hemoglobin (Hb) from bovine blood (Mw = 64.5K Da), and routine chemical reagents were from Sigma–Aldrich. Human fibrinogen was isolated [72] from pooled volunteer plasma under institutional IRB-approved human subject research protocol.[73, 74]Imprinting was performed using 11-mercapto-1-undecanol ($SH-(CH_2)_{11}-OH$; 97%, Aldrich), dimethyl sulfoxide (DMSO).

3.2.2 Gold substrate physical vapor deposition

Gold/chromium substrates were prepared by the physical vapor deposition of gold onto silicon wafers in a high-vacuum evaporator at 10^{-7} Torr. Silicon wafers substrates were preheated to 325 °C for 2 hours by a radiation heater before deposition. Evaporation rates were 0.1- 0.3 nm/s, and the final thickness of the gold films was around 100 nm.

3.2.3 MI Biosensor fabrication

In order to fabricate the gold surface with different roughness, first a 10 nm layer of chromium was deposited onto the Si substrate to facilitate adhesion, followed by a 100 nm coating of gold. The coatings were deposited on either the smooth or the rough side of the silicon substrate using electron beam evaporation in a vacuum of 10^{-7} Torr in the Cornell NanoScale Facility (CNF). The gold-coated substrate (1.5 cm × 2 cm) was rinsed with ethanol and dried under nitrogen gas. The gold electrode was then covered in Teflon tape leaving an open active circular area of 1.2 cm in diameter for imprinting. In this manner the response from different sensor electrodes could be quantitatively compared.

To make the SAM on the gold surface, different ratios of thiol/DMSO and analyte/DI were prepared. Thiol and analyte blend solutions were made as follows: the templating analyte was dissolved in de-ionized water and the alkanethiols, were dissolved in DMSO. The two solutions were mixed (19/1 [v/v], respectively) to a 100 μM final thiol concentration. The final concentration of the imprinted analytes, such as Hb, Mb, CEA, and Fb, were 0.465 μM, 1.7 μM,

0.0075 nM and 0.059 μM, respectively. For poliovirus and adenovirus were 1.5×10^8 and 5.0×10^7, respectively.

The prepared gold-coated electrode was then immersed into the analyte/thiol imprinting solution at room temperature for 2.5 hours and soaked into 1 M NaCl solution for 1 hour to remove the templating molecules.

3.2.4 Electrochemical measurements

The analytes were assayed in a beaker containing 10 mL of 1x PBS detection medium continuously stirred with a magnetic stirrer. A potentiometer (Lawson Laboratories, Model E13) was utilized to monitor the potential change of the MI biosensor. An Ag/AgCl electrode was connected to reference channel and the imprinted gold chip was connected to working electrode channel. A fixed amount of the analyte solution was pipetted, dropwise, into the detection medium, and the open circuit potential (OCP) was monitored using L-EMF DAQ software.

Electrochemical impedance spectroscopy (EIS) measurements were performed using a CHI 660d electrochemical workstation (CH Instruments) with a three electrodes system. It consists of a gold chip electrode, with or without molecular imprinting, as the working electrode, a platinum wire as the counter electrode and an Ag/AgCl electrode (BASi) as the reference electrode.

3.3 Results

3.3.1 Surface characterization

(a) Surface topography characterization was operated by AFM. In Figure 3-1 (A) (B) we show a 3D view of the AFM topographical scans of the smooth and rough gold coated silicon substrates, together with typical cross sectional scans showing how the surface morphology was analyzed. The distribution of both horizontal and vertical length scales for the roughness on the smooth and rough gold surfaces are plotted in Figure 3-1 (C) and (D), respectively. Two distinct Gaussian curves are obtained. On the smooth god surface the distribution is narrow, with the horizontal mean roughness being approximately twice as large as the vertical mean roughness of 3.4 (±0.5) nm while on the rough gold surface, the distribution is much broader with the mean horizontal spacing being approximately five time larger than the mean vertical roughness of 17 (± 5.3) nm.

Therefore, the gold surface with multi-scale roughness was easily prepared by gold PVD on smooth and rough side of silicon substrate.

(b) Surface wettability was characterized by contact angle goniometry. In Figure 3-1 (E) we show the water contact angle obtained on the two bare gold surfaces and the surfaces after they are covered with a SAM without imprinted analytes. On Both gold surfaces, although the surface physical roughness are different, the contact angles on both surfaces decrease to the same value of 23 ± 1.6 degrees confirming that they are both fully coated with identical surface chemical properties. Hence the two surfaces differ mostly in degree of topographical roughens, while their chemical properties are very similar.

3.3.2 Electrochemical characterization

The area occupied by the imprinting molecules can be determined by titrating the amount of thiols that are deposited after the analyte has been removed. It is well established that thiol molecules are adsorbed to the gold surface through strong sulfur -Au bond to form SAM via the electron transfer reaction, [19, 21]

Equation 1: $R\text{-}S\text{-}H + Au \rightarrow R\text{-}S\text{-}Au + e^- + H^+$

Therefore the thiol-Au adsorption process could be studied by observing the OCP change generated from transfer of the free electron to the gold conducting layer. In order to determine the area fraction that has no SAM cover after the analyte was removed, the electrode was re-inserted into the detection solution, and a thiol solution of 0.4 mg/ml thiols was added in the analysis chamber , while the was generated by the free electron emitted in the reaction was recorded. The data for the OCP on the bare gold and the fully covered surfaces are shown in Figure 3-1 (F).

In order to determine the OCP generated when the gold surface is fully covered by thiol molecules, the bare gold electrode was inserted into the detection solution (PBS buffer) and thiols were added till a plateau region in the OCP was reached indicating the surface was fully covered. Similarly electrodes were imprinted for different amounts of analyte and the thiol solution was added till a plateau was easily discernable in the OCP readings. The curves are shown in Figure 3-1 (F), where we see that on the smooth surface a plateau value of 120 mV was obtained when a total of 100 μM of thiols were added. Since no further increase in the OCP

response occurred when additional thiols were added, the value at the onset was taken to correspond to the OCP generated as the surface coverage was completed. Since the area exposed to the thiol solution is the same in all experiments, we can conclude that the rough side of the Si wafer exposes approximately 100 percent gold additional surface area. This additional area is required for the detection of the larger analytes and is responsible for the larger OCP responses observed.

3.3.3 Analyte introduction

In order to probe the degree to which surface roughness and analyte size resonate to maximize the open circuit potentiometric signal, both smooth and rough gold electrodes were imprinted with analytes with different dimensions. The relative sizes of the analytes used are compared to each other in Figure 3-2 (A), sorted by their vertical dimension, which ranges from 5 nm to more than 2 microns. In order to span this large range, more than 10 types of analytes were used and cover a broad gamut of biological molecules ranging from proteins, antigen, viruses, to bacteria. In Table 3-1, the sizes and the molecular weights of all the analytes we used in this study are summarized [14, 75-80].

When analyte is re-introduced, a potentiometric response occurs, or an open circuit potential (OCP) variation is established when the analyte fits accurately back into the imprinted cavity. A typical OCP vs concentration curve for hemoglobin (Hb) is shown in Figure 3-3 (B). In Figure 3-3 (B) we show the OCP for a gold electrode imprinted for Hb and where Hb or Myoglobin (Mb) are added as the analytes. Typical OCP response curve corresponding to Hb has two domains, a linear and a plateau regime. In the linear regime the imprinted spaces are rapidly being filled up with each droplet, and hence the OCP response is linear in Hb concentration. The biosensor is then calibrated and quantitative readouts of the Hb concentration in the analyte solution were obtained. The onset of the plateau region indicates when the imprinted cavities are completely filled and additional analytes no linger trigger an OCP. Concentrations in this regime can only elicit a yes/no response. Addition of Mb analyte does not engender an OCP response since the Mb molecule does not fit into the cavities produced by Hb. The lack or response for the analyte that does not match the imprint is an indication of the specificity of the detection method.

Another situation where a poor response can occur is when the size of the analyte is mismatched to the size of the niche in which it is imprinted, as illustrated in Figure 3-3 (C). In

this case when a small analyte is imprinted on a gold surface where the roughness was much bigger than the size of the analyte. In this case, the cavity is too big to be spanned by the imprinting thiols, as shown in the figure. On the other hand the cavities on the smoother surface are tight enough where selective adsorption of the thiols around the molecule can fill all space. The inverse situation is illustrated in bottom layer of Figure 3-3(C), where we have a large analyte. In this case the imprinting must be done on the rougher surface to accommodate the analyte.

3.3.4 Detection of hemoglobin under different pH

Hb is a tetramer composed of two sets of α and β subunits. It is the smallest analyst in our study, therefore, it turns out to be the best analyte to investigate how subtle conformational change can MI biosensor to differentiate. The major function of Hb is to carry oxygen, which is adsorbed in the heme. The degree of oxygenation of the molecule is a function of pH where the molecule has a resonant vibration after binding.[81-83] Therefore, the structure of Hb can change significantly with different pH in aqueous solution. In order to determine if the technique is sufficiently sensitive to detect changes in morphology alone, a pH cross test was designed to investigate the limit of biosensor. For the first group, Hb was imprinted at pH 6.5 and then detected at pH ranging from 5.0 to 8.0. For the second group, Hb was imprinted at pH 5.5 and detected at pH ranging from 4.5 to 7.0. The OCP response function for each trial is plotted in Figure 3-4 (B) Inset. The maximum OCP response is obtained when the imprint and detection are performed at the same pH value. The Maximum OCP as a function of pH was also plotted in Figure 3-4 (B) and (C). The maximum OCP values are similar for the electrode imprinted at 6.5 and at 5.5, indicating that the quality of SAM is not degraded in this pH range. In each case, the OCP has a normal distribution around the maximum value, indicating that the imprinting process can detect the subtle variation in the molecular structure. Based on the pH cross test, we proved that the sensor does not only detect chemical differences, but also purely molecular structure differences in the molecule. This kind of physical geometry variation is impossible to be detected through regular chemical analysis methods. Hence, the pH cross test of Hb biosensor proves the sensitivity of MI biosensor to differentiate subtle conformational change between protein molecular, such as misfolding protein.

3.3.5 Detection of molecular clusters: Fibrinogen and fibrin/fibrinogen complex

Fibrinogen (Fb) is a critical protein in hemostasis blood. Its structure consists of two identical halves, each formed by three non-identical poly-peptide chains, Aα, Bβ and ϒ[84, 85]. The amino termini of all six chains are disulfide-linked forming its central or E region while disulfide-linked carboxyl terminal portions of Bβ and ϒ chains and a portion of the Aα chain form its two outer or D regions. In the inactive state fibrinogen is hydrophilic and remains in the blood steam. Fb can be activated by thrombin to induce clotting by cleaving fibrinopeptides A and B. The resulting fibrin monomer self-assembles to form fibrils which progress to fiber formation by lateral contact with one another.

Many mutations of Fb have been reported that inhibit fibrin polymerization. Currently, it is common practice to test the clotting ability of a patient's blood prior to any medical proceeding. Failure to clot can have many different underlying reasons and a precise determination of the cause can be very helpful in determining how to proceed. For example, a minor fraction of circulating Fb is clottable catabolic lacking varying parts of the C terminal region of their Aalpha chains, currently termed des-alphaC fibrinogen. Maximum OCP response is compared in Figure 3-5 (A) around 60 mV OCP response was obtained on the smooth surface, while almost no OCP response can be observed on rough surface. Therefore, smooth gold surface was selected for Fb imprinting. In Figure 3-5 (B), we imprinted Fb on smooth gold surface, and cross test with normal Fb and Des αC Fb. The cartoon in the inset shows the structure of the fibrinogen, clearly, Des-αC fibrinogen molecule lose a part of Alpha chain. No obvious OCP response is observed when cross test with Des αC Fb, shows the great capacity of Fb biosensor to differentiate this mutated fibrinogen.

Then we continue to study more fibrinogen type with mutation. Soluble fibrin exists in blood in complex with three fibrinogen molecules but the exact composition or complex size is not known. This complex can be measured by clinical laboratory methods, but they are not currently used since soluble fibrin is limited clinical relevance. In Figure 3-5 (C), maximum OCP is compared for fibrinogen complex imprinted on smooth and rough side of gold surface. No OCP response is observed on smooth gold, since the fibrinogen complex is much larger than fibrinogen molecule. Therefore, the best MI effect can be obtained on rough gold surface for fibrinogen complex.

In Figure 3-5 (D), the specificity of Fb complex was evaluated. Different analytes were tested with Fb complex biosensor. Another mutant of fibrinogen complex, fibrinogen-IgG complex, was cross-tested with fibrinogen complex biosensor, around 20 mV OCP response was obtained. This number of OCP response probably comes from some regular fibrinogen complex in the sample, which means there are still some regular fibrinogen complexes in the sample. Regular fibrinogen was also tested, and no OCP response was observed. In order to test the limit of the fibrinogen complex biosensor, fibrinogen complex with a single amino acid mutation was tested, and similar OCP response was generated during the detection process, which indicates the geometry of single mutation fibrinogen complex is very close to regular fibrinogen complex, and the biosensor cannot differentiate this subtle structure difference.

3.3.6 Imprinting with viral and bacterial particles

Detection of viral particles is commonly done via either RT-PCR or sequencing of the viral RNA or DNA. Both techniques require amplification and hence cannot be done at bedside. Our method detects the entire virion, at a sensitivity level of better than 10^6 particles per ml. Here we tested the detection method for two viruses, polio and adenovirus, where, as can be seen from Figure 3-2(A), the poliovirus is much smaller than the Adenovirus, i.e., 30 nm vs 90 nm. The potentiometric responses for an electrode imprinted for poliovirus and cross-tested with poliovirus, on both the rough and smooth sides are shown in Figure 3-6 (A). The sensitivity and the OCP response are both higher on the smooth surface, even though an adequate response is also obtained on the rough surface. In this case the size of the virions, approximately 30 nm, can be fit in the region of overlap between the roughness distributions of both smooth and rough surfaces.

The OCP responses for electrodes imprinted with the adenovirus, on smooth and rough surfaces are shown in Fig 3-6 (B) inset. The much larger size of this virus, 90 nm, does not produce a significant signal on the smooth surface, while a large OCP response is observed on the rough surface. The larger size of the adenovirus, 90 nm, is close to the mean value of the rough surface, and at least 3 times larger than the mean of the smooth surface. Cross testing the electrode imprinted with adenovirus with the polio virus, as shown in Fig 3-6 (B), does not elicit an OCP, indicative of the ability of the sensor to differentiate between these two viruses.

Given the enhanced sensitivity we observed for larger analytes detected on imprinted rough gold surfaces, we tried to determine if the detection capacity could further be extended to bacteria. Two types of bacteria, S.Aureus and E.Coli, one gram positive with radius of 600nm and the other gram negative, with a radius of 2 μm, were tested. The OCP response as a function of concentration is shown in Figure 3-6 (C), for an electrode imprinted with S.Aureus and tested with both S.Aureus and E coli. A robust OCP signal is observed in both cases, indicating that, despite the large response, the MI biosensor no longer has specificity for bacteria. In this case, the diameters of both particles are much larger than the mean roughness of the rough gold surface, and hence can not make imprints with sufficient sensitivity to the shape of the bacteria. If we overlay the two types of bacteria on the drawing of the rough gold surface, the niche created covers less than 25% of the area of both types of bacteria. Hence even though these two bacteria have very different structures, the imprinted area does not provide a sufficiently large area to positively identify the analyte. The OCP response obtained with bacteria is non-specific to either type of bacteria or the roughness provided by either the smooth or the rough gold surfaces. Electrodes with larger roughness possibly produced via micolithographic methods are currently being attempted.

3.4 Discussion

Taken together these results imply that the process through which proteins or viruses are templated, is not a two dimensional function only of the height of the SAM, as was initially postulated by Zhou[12]. Rather, the template is three-dimensional, as shown in Figures 3-3 (C). The analyte is enveloped within the niches on the gold surface created by the substrate roughness. The SAM then forms around the analyte as it fills in and coats the wall of the niche surrounding the analyte. When the analyte is washed off, it leaves behind a three dimensional imprinted cavity complimentary with imprinted molecule, which is highly specific to the conformation of the analyte. In this case the size of the niche has to be commensurate with the dimensions of the analyte. If the niche is too large, i.e. the surface roughness is too large and the SAM layer, which is attached to the surfaces of the wall surrounding the analyte, does not come in contact with the imprinting molecule and hence fails to form an identifying pattern. Similarly, if the analyte is much larger than the niche dimensions, then only a small fraction of its surface is imprinted, and

the template is not specific enough to the analyte. On the scale of Figure 3-2(A) we also mark with arrows the measured roughness of the smooth and rough sides of the electrode, as well as the range of roughness available on the respective surfaces. A broad spectrum of roughness is available on each surface allows for the imprinting of analytes for which the precise dimensions are not known. In fact the small region of overlap explains the ability to detect some of the molecules, such as the poliovirus on either of the two substrates. The OCP though is larger on the rough surface due to the increased surface area available for the imprint.

In Figure 3-2 (A) there is a critical dimension exists which separates the analytes that are best detected by the rough surface from those that are best detected on the smooth surface. Hence these results indicate that future improvements to the biosensor and in particular improving its ability to detect bacteria can be implemented via lithographic methods, where the roughness is exactly tailored to the analyte.

3.5 Conclusion

In conclusion we have shown that MI biosensors is capable of applying to a broad scale of biological molecules, such as proteins, viruses, and bacteria, ranging in size from several nanometers to hundreds of nanometers. In the case of 2D imprinting, the height of the SAM, 1.2 nm, dictated the maximum dimensions of the imprinted molecule. Here we present a model for 3D imprinting, where the analyte is sequestered within a niche within the surface roughness. The SAM is then assembled on the walls of the niche, forming a three dimensional pattern of the analyte. This then imposes the boundary conditions upon the surface morphology, where the walls must be sufficiently close to the molecule such that the SAM can form around it and mold to its contour. When this condition is satisfied, the MI method is very sensitive and was shown to differentiate between different conformation of one molecule due to changes in pH , and positively identify viruses in liquids containing as little as 10^6 particles.

Table 3-1. Summary of the size and molecule weight of analyte in this study.

Analyte	$M_w(\times 10^3)$	Dimension (nm)	Shape	Reference
Mb	17.6	3.5×2×4.5	Rectangle	40
Hb	64.5	5×5×5	Rectangle	41
CEA	200	8×28†	Cylinder	42
Fb	340	9×6×47	Rectangle	40
Poliovirus	N/A	20 ‡	Sphere	43
Adenovirus	N/A	90 ‡	Sphere	44
S. Aureus	N/A	600 ‡	Sphere	45
E.Coli	N/A	500×2000†	Cylinder	46

† The shape of molecule is cylinder, the first number represents the radius of undersurface, and the second number represents the height of cylinder.

‡ The shape of the molecules is sphere; the number represents the diameter of the sphere.

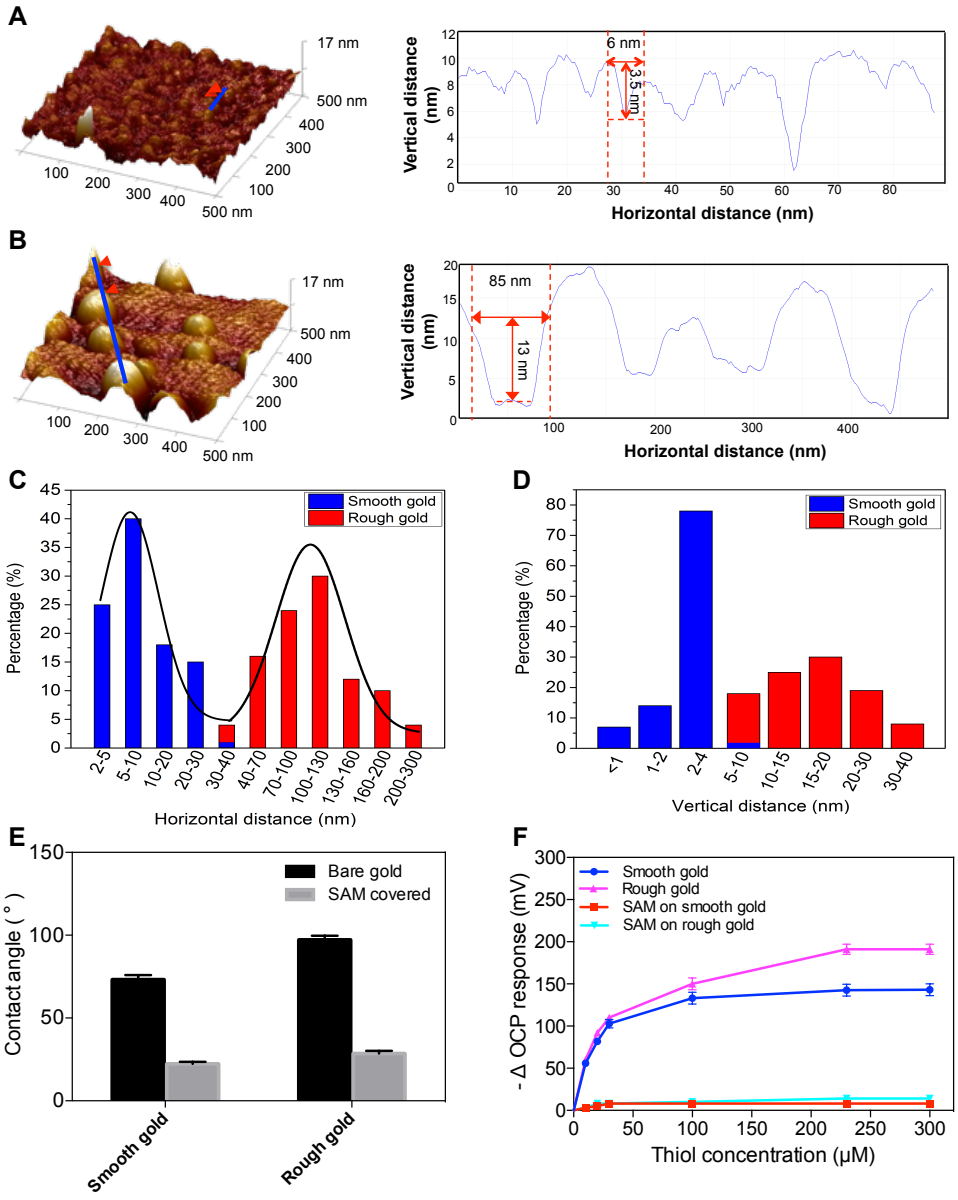

Figure 3-1. Surface characterization of multi-scale roughness gold surfaces. AFM topographical scan and the associated cross sectional analysis for A) smooth and B) rough gold surfaces. Further description of the surfaces by histogram of C) horizontal and D) vertical surface roughness for smooth and rough gold surfaces is shown. Comparison between smooth and rough surfaces before (bare gold) and after (SAM covered) SAM formation characterized by E) contact angle and F) potentiometric titration with thiol solution. Similar chemistry property was found on

both smooth and rough gold surfaces after SAM formation, despite of the large physical roughness difference between them.

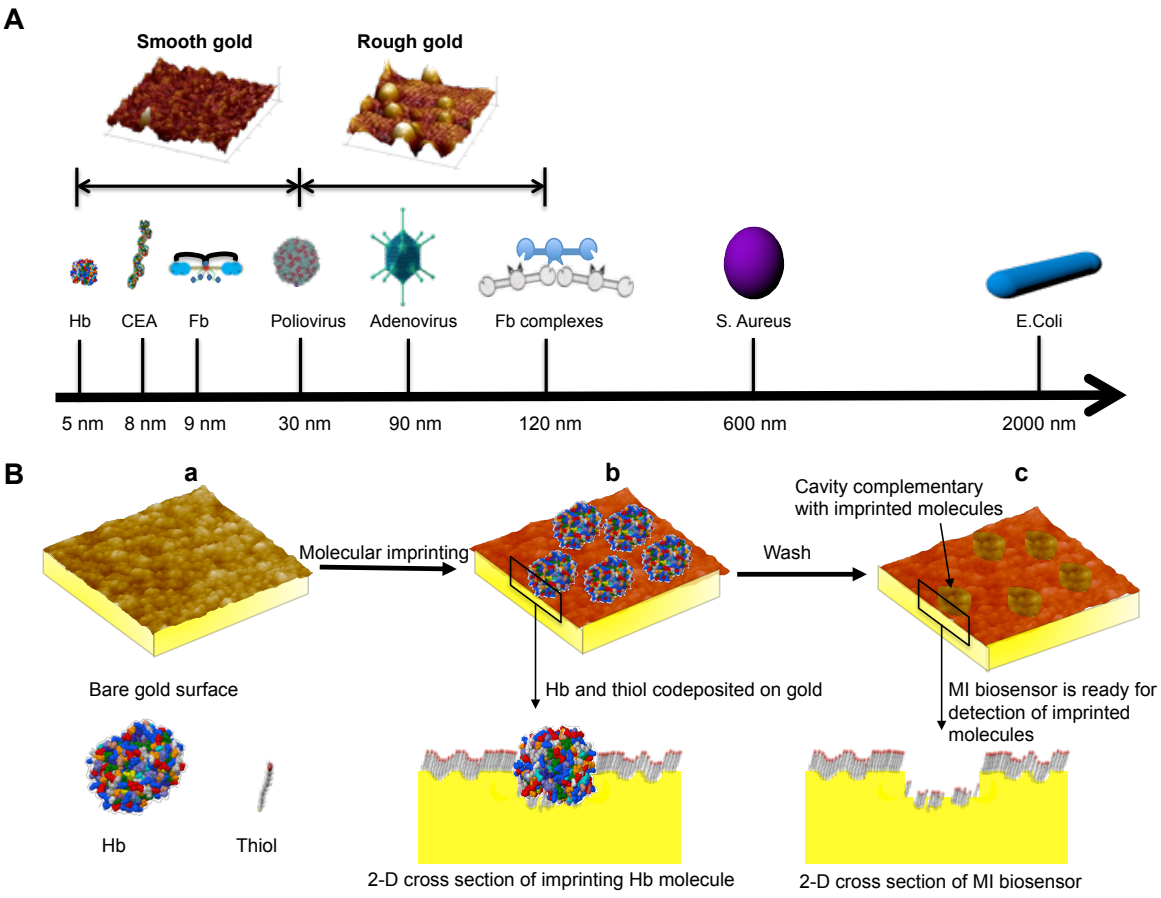

Figure 3-2. A summary of possible analytes and fabrication process of the MI biosensor . (A) Size distribution of the possible analytes in this study, including protein, antigen, virus and bacteria in different sizes, as plotted on a nanometer scale chart. (B) Schematic illustration and cross-sectional of the 3D MI biosensor fabrication process. The red-color layer represents SAM coverage.

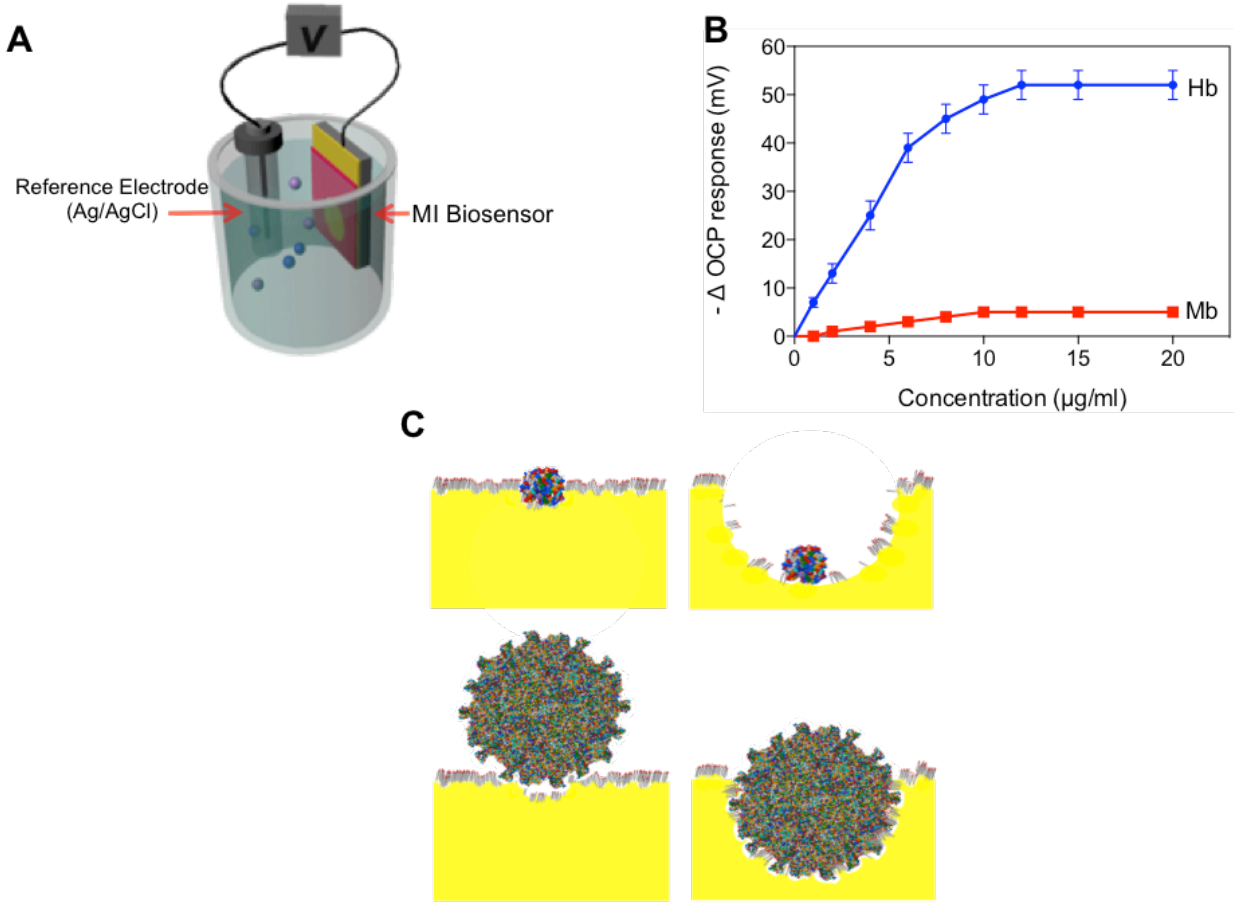

Figure 3-3. OCP detection method on multi-scale roughness surface. (A) A schematic illustration of the OCP detection set up. (B) Selectivity test using Hb MI biosensor imprinted on smooth surface to detect Hb and Mb. (C) Schematic representation of the fitting principle of small and large analytes into imprints on multi-scale roughness surface. A good fit occurs only when the analyte dimension matches the gold surface roughness.

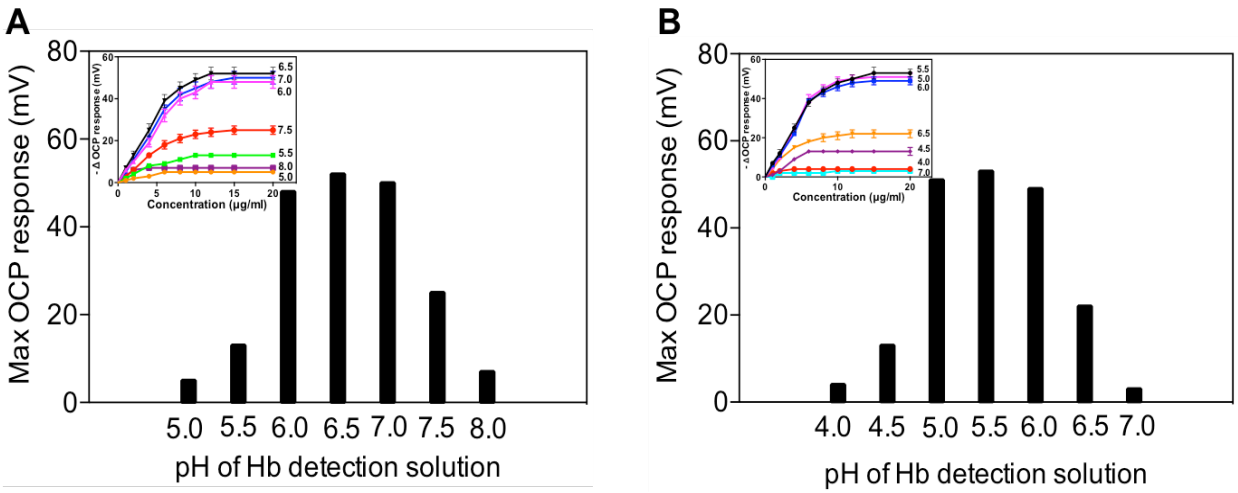

Figure 3-4. pH cross test of Hb biosensor on smooth gold surface. Hb biosensor was imprinted at A) pH = 6.5 and detected at pH 5.0 to 8.0 as well as at B) pH =5.5 and detected at pH 4.0 to 7.0. Hb is known to change its conformation and size to subtle alteration of pH values. Two Hb biosensors at either pH=6.5 or pH=5.5 were prepared. The maximum OCP response of Hb to each biosensor was studied.

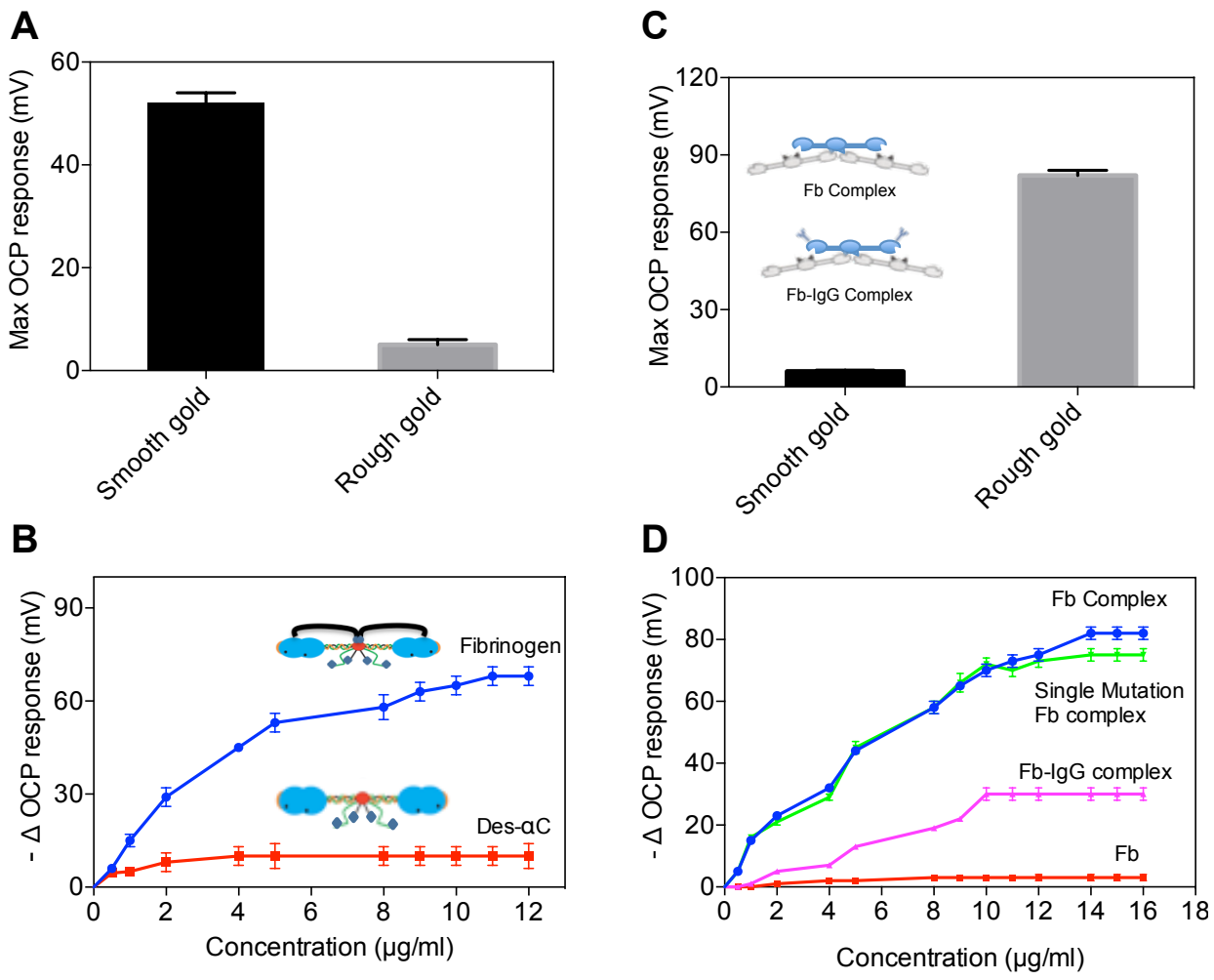

Figure 3-5. Detection of Fb and Fb complex in different size scales with various MI biosensors. (A) Maximum OCP response of Fb in small size to Fb biosensor imprinted on either smooth or rough surfaces and (B) further selectivity test of Fb MI biosensor imprinted on smooth surface to detect Fb. Des-αC Fb with same size of Fb was chosen as a control, but showed little response. Structures of normal Fb and Des-αC Fb were shown in the insets, indicating the similar size of both analytes, but with subtle difference in conformation. (C) Maximum OCP responses of Fb complex in large size to Fb complex biosensor imprinted on either smooth or rough surfaces and (D) further selectivity test of Fb complex biosensor imprinted on rough surface to detect Fb complex, Fb complex with single amino acid mutation, Fb-IgG complex and Fb respectively.

Structures of Fb-IgG complex and Fb complex were shown in the insets of (C). Fb complex refers to a cluster of 3 Fb molecules. Fb complex with single amino acid mutation was unable to be differentiated, indicating the detection limit of MI biosensor.

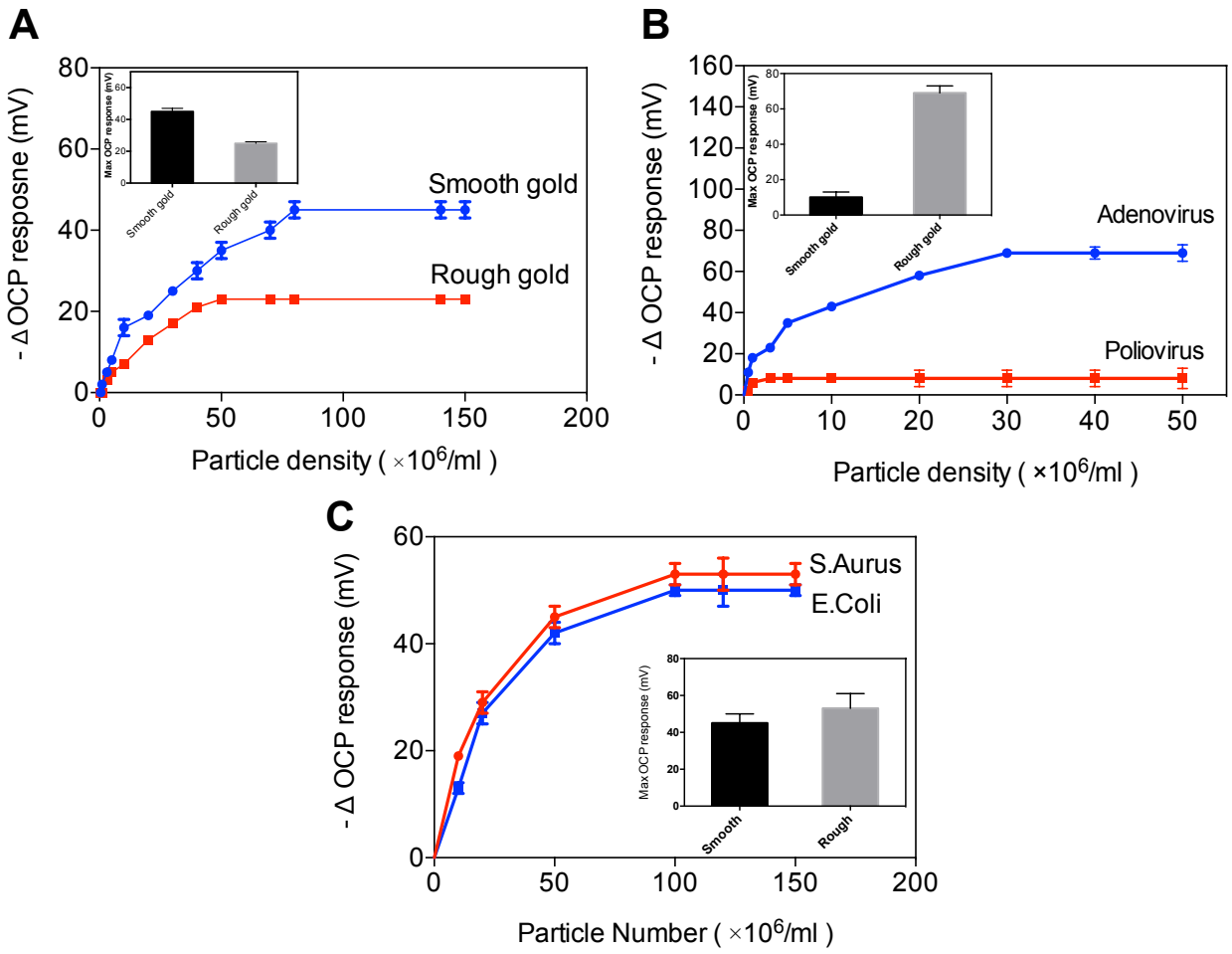

Figure 3-6. Detection of virus and bacteria with MI biosensor. (A) OCP responses of poliovirus to poliovirus biosensor imprinted on smooth and rough gold surface. Comparison of maximum OCP response of poliovirus to poliovirus biosensor imprinted on smooth and rough gold surfaces respectively was shown in insets. (B) Selectivity test using adenovirus MI biosensor imprinted on smooth and rough gold surface to detect adenovirus and poliovirus. Comparison of maximum OCP response of adenovirus to adenovirus imprinted on smooth and rough gold surfaces. (C) Selectivity test using S. Aureus biosensor imprinted on smooth and rough gold surfaces to detect S.Aureus and E.Coli. Comparison of maximum OCP response of S.Aureus to S.Aureus biosensor imprinted on smooth and rough gold surfaces was also shown in insets. It is shown that the bacteria biosensor lost its specificity since the large size of the analyte.

Reference

1. Mohanty, S.P. and E. Kougianos, *Biosensors: a tutorial review.* Potentials, IEEE, 2006. **25**(2): p. 35-40.
2. Kissinger, P.T., *Biosensors—a perspective.* Biosensors and Bioelectronics, 2005. **20**(12): p. 2512-2516.
3. Scheller, F.W., et al., *Research and development in biosensors.* Curr Opin Biotechnol, 2001. **12**(1): p. 35-40.
4. Ma, X.H., et al., *A Review on Bio-macromolecular Imprinted Sensors and Their Applications.* Chinese Journal of Analytical Chemistry, 2016. **44**(1): p. 152-159.
5. Bolisay, L.D., J.N. Culver, and P. Kofinas, *Molecularly imprinted polymers for tobacco mosaic virus recognition.* Biomaterials, 2006. **27**(22): p. 4165-4168.
6. Kriz, D., O. Ramström, and K. Mosbach, *Peer Reviewed: Molecular Imprinting: New Possibilities for Sensor Technology.* Analytical Chemistry, 1997. **69**(11): p. 345A-349A.
7. Turner, N.W., et al., *From 3D to 2D: A review of the molecular imprinting of proteins.* Biotechnology Progress, 2006. **22**(6): p. 1474-1489.
8. Piletsky, S.A., N.W. Turner, and P. Laitenberger, *Molecularly imprinted polymers in clinical diagnostics - Future potential and existing problems.* Medical Engineering & Physics, 2006. **28**(10): p. 971-977.
9. Ou, S.H., et al., *Polyacrylamide gels with electrostatic functional groups for the molecular imprinting of lysozyme.* Analytica Chimica Acta, 2004. **504**(1): p. 163-166.
10. Tabushi, I., et al., *Supramolecular sensor based on SnO 2 electrode modified withoctadecylsilyl monolayer having molecular binding sites.* Tetrahedron letters, 1987. **28**(37): p. 4299-4302.
11. Zhou, Y.X. and K. Levon, *Potentiometric sensor for dipicolinic acid.* Abstracts of Papers of the American Chemical Society, 2004. **228**: p. U119-U119.
12. Zhou, Y.X., B. Yu, and K. Levon, *Potentiometric sensing of chiral amino acids.* Chemistry of Materials, 2003. **15**(14): p. 2774-2779.
13. Brugge, W.R., et al., *Diagnosis of pancreatic cystic neoplasms: A report of the cooperative pancreatic cyst study.* Gastroenterology, 2004. **126**(5): p. 1330-1336.
14. Boehm, M.K., et al., *Extended glycoprotein structure of the seven domains in human carcinoembryonic antigen by X-ray and neutron solution scattering and an automated curve fitting procedure: Implications for cellular adhesion.* Journal of Molecular Biology, 1996. **259**(4): p. 718-736.
15. Slayter, H.S. and J.E. Coligan, *Electron microscopy and physical characterization of the carcinoembryonic antigen.* Biochemistry, 1975. **14**(11): p. 2323-2330.
16. Ganesh, V., et al., *Self-assembled monolayers (SAMs) of alkoxycyanobiphenyl thiols on gold--a study of electron transfer reaction using cyclic voltammetry and electrochemical impedance spectroscopy.* J Colloid Interface Sci, 2006. **296**(1): p. 195-203.
17. Zhang, X.F., et al., *Creating Protein-Imprinted Self-Assembled Monolayers with Multiple Binding Sites and Biocompatible Imprinted Cavities.* Journal of the American Chemical Society, 2013. **135**(25): p. 9248-9251.
18. Blomquist, M., et al., *Electrochemical and spectroscopic study on thiolation of polyaniline.* Electrochimica Acta, 2013. **90**: p. 604-614.
19. Cohen-Atiya, M. and D. Mandler, *Studying thiol adsorption on Au, Ag and Hg surfaces by potentiometric measurements.* Journal of Electroanalytical Chemistry, 2003. **550**: p. 267-276.

20. Flynn, N.T., et al., *Long-term stability of self-assembled monolayers in biological media.* Langmuir, 2003. **19**(26): p. 10909-10915.
21. Vericat, C., et al., *Self-assembled monolayers of thiols and dithiols on gold: new challenges for a well-known system.* Chemical Society Reviews, 2010. **39**(5): p. 1805-1834.
22. Yaqub, S., U. Latif, and F.L. Dickert, *Plastic antibodies as chemical sensor material for atrazine detection.* Sensors and Actuators B-Chemical, 2011. **160**(1): p. 227-233.
23. Lenain, P., et al., *Affinity sensor based on immobilized molecular imprinted synthetic recognition elements.* Biosensors & Bioelectronics, 2015. **69**: p. 34-39.
24. Sun, G.Q., et al., *Photoelectrochemical sensor for pentachlorophenol on microfluidic paper-based analytical device based on the molecular imprinting technique.* Biosensors & Bioelectronics, 2014. **56**: p. 97-103.
25. Zhang, Q., et al., *A polyaniline based ultrasensitive potentiometric immunosensor for cardiac troponin complex detection.* Biosensors & Bioelectronics, 2015. **72**: p. 100-106.
26. Wang, Y.T., et al., *A potentiometric protein sensor built with surface molecular imprinting method.* Biosensors & Bioelectronics, 2008. **24**(1): p. 162-166.
27. Wang, Y.T., et al., *Potentiometric sensors based on surface molecular imprinting: Detection of cancer biomarkers and viruses.* Sensors and Actuators B-Chemical, 2010. **146**(1): p. 381-387.
28. Zhou, Y.X., B. Yu, and K. Levon, *Chiral surface imprinting: Integrated recognition and transduction.* Abstracts of Papers of the American Chemical Society, 2003. **225**: p. U128-U128.
29. Moulton, S.E., et al., *Investigation of protein adsorption and electrochemical behavior at a gold electrode.* Journal of Colloid and Interface Science, 2003. **261**(2): p. 312-319.
30. Chen, J.H., et al., *UV-nanoimprint lithography as a tool to develop flexible microfluidic devices for electrochemical detection.* Lab on a Chip, 2015. **15**(14): p. 3086-3094.
31. Vashist, S.K., et al., *Emerging Technologies for Next-Generation Point-of-Care Testing.* Trends Biotechnol, 2015. **33**(11): p. 692-705.
32. Wang, J., *Electrochemical biosensors: Towards point-of-care cancer diagnostics.* Biosensors & Bioelectronics, 2006. **21**(10): p. 1887-1892.
33. Kost, G.J., *Goals, guidelines and principles for point-of-care testing.* Kost GJ (ed), 2002: p. 3-12.
34. Wang, J., *Survey and summary from DNA biosensors to gene chips.* Nucleic Acids Research, 2000. **28**(16): p. 3011-3016.
35. Laksanasopin, T., et al., *A smartphone dongle for diagnosis of infectious diseases at the point of care.* Sci Transl Med, 2015. **7**(273): p. 273re1.
36. Zhang, Q., et al., *Surface Functionalization of Ion-Sensitive Floating-Gate Field-Effect Transistors With Organic Electronics.* Ieee Transactions on Electron Devices, 2015. **62**(4): p. 1291-1298.
37. Levon, K., et al., *Electrochemical Monitoring of the Well‐Being of Cells.* Electrochemical Processes in Biological Systems, 2015: p. 213-230.
38. Mak, W.C., et al., *Electrochemical bioassay utilizing encapsulated electrochemical active microcrystal biolabels.* Anal Chem, 2005. **77**(9): p. 2835-41.
39. Mathur, A., et al., *Development of a Biosensor for Detection of Pleural Mesothelioma Cancer Biomarker Using Surface Imprinting.* Plos One, 2013. **8**(3).

40. Paik, W.K., et al., *Electrochemical reactions in adsorption of organosulfur molecules on gold and silver: Potential dependent adsorption.* Langmuir, 2000. **16**(26): p. 10198-10205.
41. Prabhu, A., et al., *Investigation of Protein Binding With All Solid-State Ion-Selective Electrodes.* Electroanalysis, 2013. **25**(8): p. 1887-1894.
42. Ricci, F., G. Adornetto, and G. Palleschi, *A review of experimental aspects of electrochemical immunosensors.* Electrochimica Acta, 2012. **84**: p. 74-83.
43. Rivas, G.A., M.L. Pedano, and N.F. Ferreyra, *Electrochemical biosensors for sequence-specific DNA detection.* Analytical Letters, 2005. **38**(15): p. 2653-2703.
44. Rizal, B., et al., *Nanocoax-based electrochemical sensor.* Anal Chem, 2013. **85**(21): p. 10040-4.
45. Thevenot, D.R., et al., *Electrochemical biosensors: recommended definitions and classification.* Biosens Bioelectron, 2001. **16**(1-2): p. 121-31.
46. Wilson, M.S. and W.Y. Nie, *Electrochemical multianalyte immunoassays using an array-based sensor.* Analytical Chemistry, 2006. **78**(8): p. 2507-2513.
47. Rothberg, J.M., et al., *An integrated semiconductor device enabling non-optical genome sequencing.* Nature, 2011. **475**(7356): p. 348-352.
48. He, P.A., Y. Xu, and Y.Z. Fang, *A review: Electrochemical DNA biosensors for sequence recognition.* Analytical Letters, 2005. **38**(15): p. 2597-2623.
49. Dias, J.T., et al., *Minimizing antibody cross-reactivity in multiplex detection of biomarkers in paper-based point-of-care assays.* Nanoscale, 2016. **8**(15): p. 8195-201.
50. Choi, J.R., et al., *An integrated paper-based sample-to-answer biosensor for nucleic acid testing at the point of care.* Lab on a Chip, 2016. **16**(3): p. 611-621.
51. Miao, P., Y. Tang, and J. Yin, *MicroRNA detection based on analyte triggered nanoparticle localization on a tetrahedral DNA modified electrode followed by hybridization chain reaction dual amplification.* Chem Commun (Camb), 2015. **51**(86): p. 15629-32.
52. Miao, P., et al., *Nuclease assisted target recycling and spherical nucleic acids gold nanoparticles recruitment for ultrasensitive detection of microRNA.* Electrochimica Acta, 2016. **190**: p. 396-401.
53. Miao, P., et al., *Ultrasensitive electrochemical detection of microRNA with star trigon structure and endonuclease mediated signal amplification.* Biosens Bioelectron, 2015. **63**: p. 365-70.
54. Chen, J.H., et al., *Electrochemical nanoparticle-enzyme sensors for screening bacterial contamination in drinking water.* Analyst, 2015. **140**(15): p. 4991-4996.
55. Chen, J.H., et al., *Bacteriophage-based nanoprobes for rapid bacteria separation.* Nanoscale, 2015. **7**(39): p. 16230-16236.
56. Huang, Y.X., et al., *Nanoelectronic biosensors based on CVD grown graphene.* Nanoscale, 2010. **2**(8): p. 1485-1488.
57. Duzgun, A., et al., *Protein Detection with Potentiometric Aptasensors: A Comparative Study between Polyaniline and Single-Walled Carbon Nanotubes Transducers.* Scientific World Journal, 2013.
58. Zhou, Y., et al., *Potentiometric monitoring DNA hybridization.* Biosensors & Bioelectronics, 2009. **24**(11): p. 3275-3280.

59. Wang, Y.T., et al., *COLL 32-A potentiometric sensor for the Ddtection of proteins or viruses built with surface molecular imprinting method.* Abstracts of Papers of the American Chemical Society, 2007. **234**.
60. Kell, A.J., et al., *The development of a silica nanoparticle-based label-free DNA biosensor.* Nanoscale, 2011. **3**(9): p. 3747-3754.
61. Dai, Z., et al., *A label-free electrochemical assay for quantification of gene-specific methylation in a nucleic acid sequence.* Chemical Communications, 2012. **48**(12): p. 1769-1771.
62. Chen, J., et al., *Colorimetric Detection of Escherichia coli Based on the Enzyme-Induced Metallization of Gold Nanorods.* Small, 2016.
63. Fukazawa, K., et al., *Direct observation of selective protein capturing on molecular imprinting substrates.* Biosensors & Bioelectronics, 2013. **40**(1): p. 96-101.
64. Guo, Y., et al., *Detection of the Factors That Influence the Correlation of Target Volumes for Primary Esophageal Cancer Based on PET-CT and End-Expiration Phase of 4-Dimensional CT in Radiation Treatment.* International Journal of Radiation Oncology Biology Physics, 2014. **90**: p. S342-S343.
65. Karimian, N., et al., *An ultrasensitive molecularly-imprinted human cardiac troponin sensor.* Biosensors & Bioelectronics, 2013. **50**: p. 492-498.
66. Levon, K. and Y.X. Zhou, *Electrochemical detection of biological agents.* Abstracts of Papers of the American Chemical Society, 2004. **227**: p. U453-U453.
67. Li, L., et al., *A 3D origami electrochemical immunodevice based on a Au@Pd alloy nanoparticle-paper electrode for the detection of carcinoembryonic antigen.* Journal of Materials Chemistry B, 2014. **2**(38): p. 6669-6674.
68. Flavin, K. and M. Resmini, *Imprinted nanomaterials: a new class of synthetic receptors.* Analytical and Bioanalytical Chemistry, 2009. **393**(2): p. 437-444.
69. Bosserdt, M., et al., *Microelectrospotting as a new method for electrosynthesis of surface-imprinted polymer microarrays for protein recognition.* Biosensors & Bioelectronics, 2015. **73**: p. 123-129.
70. Vlatakis, G., et al., *Drug Assay Using Antibody Mimics Made by Molecular Imprinting.* Nature, 1993. **361**(6413): p. 645-647.
71. Ganesh, V., et al., *Self-assembled monolayers (SAMS) of alkoxycyanobiphenyl thiols on gold - A study of electron transfer reaction using cyclic voltammetry and electrochemical impedance spectroscopy.* Journal of Colloid and Interface Science, 2006. **296**(1): p. 195-203.
72. Mosesson, M.W., et al., *Human fibrinogen of relatively high solubility. Comparative biophysical, biochemical, and biological studies with fibrinogen of lower solubility.* Biochemistry, 1967. **6**(10): p. 3279-87.
73. Mosesson, M.W. and S. Sherry, *Preparation and Properties of Human Fibrinogen of Relatively High Solubility.* Biochemistry, 1966. **5**(9): p. 2829-&.
74. Galanakis, D., et al., *Non-enzymatic fibrinogen self-assembly unveiled.* J Thromb Hemost 2015;. **13**(S2, Abstr. PO 202): p. 581.
75. Erickson, H.P., *Size and Shape of Protein Molecules at the Nanometer Level Determined by Sedimentation, Gel Filtration, and Electron Microscopy.* Biological Procedures Online, 2009. **11**(1): p. 32-51.
76. Ordway, G.A. and D.J. Garry, *Myoglobin: an essential hemoprotein in striated muscle.* Journal of Experimental Biology, 2004. **207**(20): p. 3441-3446.

77. Cello, J., A.V. Paul, and E. Wimmer, *Chemical synthesis of poliovirus cDNA: Generation of infectious virus in the absence of natural template.* Science, 2002. **297**(5583): p. 1016-1018.
78. Spector, D.J., *Default assembly of early adenovirus chromatin.* Virology, 2007. **359**(1): p. 116-125.
79. Kluytmans, J., A. vanBelkum, and H. Verbrugh, *Nasal carriage of Staphylococcus aureus: Epidemiology, underlying mechanisms, and associated risks.* Clinical Microbiology Reviews, 1997. **10**(3): p. 505-&.
80. Reshes, G., et al., *Cell shape dynamics in Escherichia coli.* Biophysical Journal, 2008. **94**(1): p. 251-264.
81. Mahato, M., et al., *pH Induced Structural Modulation and Interfacial Activity of Hemoglobin at the Air/Water Interface.* Journal of Physical Chemistry B, 2010. **114**(1): p. 495-502.
82. Hook, F., et al., *Structural changes in hemoglobin during adsorption to solid surfaces: Effects of pH, ionic strength, and ligand binding.* Proceedings of the National Academy of Sciences of the United States of America, 1998. **95**(21): p. 12271-12276.
83. Samuelsen, E.N., A.K. Imsland, and O. Brix, *Oxygen binding properties of three different hemoglobin genotypes in turbot (Scophthalmus maximus Rafinesque): Effect of temperature and pH.* Fish Physiology and Biochemistry, 1999. **20**(2): p. 135-141.
84. Koo, J., et al., *Control of anti-thrombogenic properties: surface-induced self-assembly of fibrinogen fibers.* Biomacromolecules, 2012. **13**(5): p. 1259-68.
85. Koo, J., et al., *Evaluation of fibrinogen self-assembly: role of its alphaC region.* J Thromb Haemost, 2010. **8**(12): p. 2727-35.